Renewable Energy 272 (2026) 126005

Contents lists available at ScienceDirect

Renewable Energy

journal homepage: www.elsevier.com/locate/renene

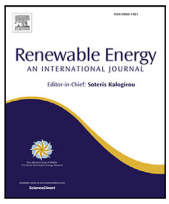

Mixed Wave Energy arrays, re-thinking wave array configurations: A hydrodynamics based approach

Vaibhav Raghavan *, Andrei V. Metrikine, George Lavidas

Delft University of Technology, Stevinweg 1, Delft, 2628 CN, Zuid Holland, Netherlands

ARTICLE INFO

Keywords:
Mixed arrays
HAMS-MREL
Weakly non-linear
Control
Wave energy

ABSTRACT

Wave energy arrays are essential for reducing the Levelised Cost of Energy, yet the performance of traditional mono-device arrays is often limited by destructive hydrodynamic interactions and directional sensitivity. This work focuses on "mixed arrays," wherein different types and geometries of wave energy converters operating in different degrees of freedom (point Absorber and a flap) are deployed within the same array to exploit complementary device dynamics, whilst reducing spatial requirements. Using a weakly non-linear frequency-domain model utilising the solver HAMS-MREL, a systematic comparison is performed across 3360 cases considering varying array sizes, spacings, wave directions, and control strategies (active and passive). Comparison of array performance is based on the well known q-factor and a new geometry dependent metric (M-factor). The results demonstrate that mixed arrays can outperform mono-device arrays by leveraging favourable hydrodynamic cross-coupling and radiated wave-field alignment. For a 10-device staggered configuration, mixed arrays achieved a peak q-factor of 1.6 and an M-factor of 2.25 under regular waves, showing a 175% increase in point absorber heave response under displacement constraints and 34% increase in flap excitation forces. Performance is sensitive to the spacing-to-wavelength ratio, mixed arrays exhibit superior directional robustness, and reduced efficiency collapse compared to mono-flap arrays. The findings suggest that mixed-device configurations can provide a robust alternative for optimising energy capture, reducing spatial requirements, offering new collaboration opportunities and contributing to the viability of wave energy arrays.

1. Introduction

Wave energy could theoretically supply more than twice global electricity demand, owing to its high power density of 2–10 kW/m at intermediate and shallow depths, compared to 0.4–0.6 kW/m^2 for wind and 0.1–0.2 kW/m^2 for solar [1]. Waves are also more predictable and available year-round than most renewables. These attributes underpin EU targets of 1 GW of wave energy by 2030 and 40 GW by 2050 [2], with the UK leading in resource, followed by the United States, Chile, Australia, and Portugal [3]. Meeting these targets requires faster technological progress and supportive policy.

The economics of WECs reflect their pre-commercial status: capital-intensive, with a wide LCOE spread [4]. CAPEX varies by depth and device, broadly 2.5–6.0 million €/MW [4], with finer breakdowns of 5, 4, and 3 million €/MW for farshore, nearshore, and shallow-water devices [5]. Offshore wind remains cheaper at around 101 €/MWh in high-energy seas [4], but wave energy compares favourably with floating solar (10 million €/MW, range 6–16) [5] and with offshore solar in the North Sea (203–407 €/MWh) [6].

Reaching the EU targets at competitive LCOE requires large-scale array deployment, where experience curves drive cost reductions [4,5]. Optimal device selection in moderate-resource sites could bring LCOE to 60–150 €/MWh under favourable discount rates.

WEC design must capture the complex, non-linear physics of wave-structure interaction (Hydrostatic, viscous, and mooring loads) across a broad absorption bandwidth while surviving storms. This typically drives conservative design margins, higher structural mass, and inflated CAPEX.

Several devices are nearing commercial array deployment. Corpower's HiWave-5 project will test a four-WEC array (one C4 and three C5) off Aguçadoura, Portugal, while the ONDEP project plans a 2 MW Waveroller array off Peniche within five years. Studying such arrays therefore demands computationally efficient tools for multi-body wave-structure hydrodynamics.

Mono-arrays (multiple identical devices within an array) dominate both academic study and commercial deployment. Numerous experimental and numerical studies address hydrodynamics, power, and

* Corresponding author.
E-mail address: v.raghavan@tudelft.nl (V. Raghavan).

https://doi.org/10.1016/j.renene.2026.126005
Received 25 February 2026; Received in revised form 26 May 2026; Accepted 27 May 2026
Available online 8 June 2026

layout optimisation for Point Absorbers (PAs) [7–9], flaps [10,11], attenuators [12,13], and Oscillating Water Columns (OWCs) [14], using methods ranging from frequency-domain BIEM to high-fidelity CFD such as SPH.

Extracting more power per device boosts energy density and efficiency, motivating the study of array configurations in which the devices differ from one another in some respect. Such configurations can be grouped into three categories beyond the mono case, distinguished by what is varied across the devices and, crucially, by the structure of the radiated wave field that governs hydrodynamic interactions. Heterogeneous arrays keep the device type and dominant degree of freedom (DOF) fixed while varying device size, draft, or both, so the radiated wave fields share the same structural form but differ in amplitude and characteristic frequency. Hybrid arrays, as defined by Zheng et al. [14,15], combine devices of different working principles (e.g. oscillating water columns and point absorbers) that nonetheless share the same dominant DOF and similar geometries; although the energy-extraction mechanisms differ, the radiated wave fields share the same structural form because they arise from the same mode of motion.

Mixed arrays, the subject of the present work, combine devices with different geometries and different dominant DOFs, and therefore different working principles, producing fundamentally different radiated wave-field structures within the same array. In the configurations studied here, point absorbers radiate via heave (approximately axisymmetric wave field) and oscillating surge flaps radiate via pitch about a bottom hinge (strongly directional, cardioid-like wave field perpendicular to the flap length). This categorisation is motivated by the physics of array interactions rather than by terminology: the dominant DOF of each device determines the structure of its radiation pattern, and this in turn governs how devices exchange energy and how the array responds to directional incident waves.

Heterogeneous arrays have been investigated in several recent works. Goteman [16], using multiple scattering with WAMIT coefficients, found that mixing two cylindrical PAs with moonpools and two without (with varying inner/outer radii) yielded 2.9% more power than mono-arrays.

Ermakov et al. [17] applied a control co-design approach with displacement constraints in the frequency domain (Ansys AQWA BIEM) to heterogeneous arrays of 3–5 cylindrical PAs under multi-directional wind-waves, reporting power gains of 37% (3 WECs) to 72.2% (5 WECs).

Abdulkadir et al. [18] performed a frequency-domain optimisation of heterogeneous arrays (varying diameter) of cylindrical devices using a time-domain model with Power-Constrained Bang-Singular-Bang (PCBSB) control. Detailed simulation of homogeneous and heterogeneous arrays showed an average performance improvement of 6.6%, 20.02%, and 9.71% for 3, 5, and 7 devices for a representative wave period of 6 s and wave height of 0.82 m.

Hybrid arrays were introduced by Zheng et al. [15] in a wave-structure interaction analysis of an array combining two oscillating water columns (OWCs) and two cylindrical point absorbers (PAs). In the same line of work, Zheng et al. [14] introduced the H-factor to quantify the power-capture performance of such configurations relative to their mono-type equivalents, reporting H-factor values as high as 1.6 for some wave periods. The OWC–PA combination is an example of devices with different working principles, that nonetheless share the same dominant DOF: both the OWC chamber (with its internal water column) and the PA buoy respond predominantly in heave, producing approximately axisymmetric radiated wave fields governed by similar Bessel/Hankel structures of the heave radiation potential. The hybrid configuration therefore combines two distinct energy-extraction principles while preserving the wave-field structure characteristic of heave-mode arrays.

The present work investigates mixed wave energy arrays, in which the constituent devices differ in geometry, dominant DOF and working principle. In the configurations studied here, PAs (heave-dominated) and oscillating surge flaps (pitch-dominated) are deployed within the same array, with axisymmetric and strongly directional radiation patterns respectively. The interaction patterns that arise from combining these complementary radiation structures differ qualitatively from those of mono, heterogeneous, or hybrid arrays and form the central object of analysis in this paper. The distinction is not merely terminological: it has direct consequences for array performance, as demonstrated in Section 3, where mono-flap arrays collapse to $q = 0$ at perpendicular incidence while mixed PA–flap arrays maintain non-zero q-factors across all incidence directions—a robustness that follows directly from the axisymmetric PA radiation filling the directional gap in the flap radiation pattern.

The mixed-array concept builds on earlier studies that have demonstrated the benefits of modal or spatial diversity in wave energy systems. Li et al. [19] and Westcott et al. [20] evaluated the performance of PA arrays placed in front of a reflecting wall, exploiting spatial diversity to broaden the array response. Multi-DOF devices such as the 4-DOF Mocean attenuator [21] have shown that coupling modes with distinct natural frequencies produces a broad-banded response and enhanced power absorption. The mixed-array concept extends these ideas by introducing modal diversity at the *device level*, combining WECs with different dominant DOFs within a single array rather than coupling multiple modes within a single device.

While most previous studies on hybrid and heterogeneous arrays assess performance through power-based comparisons with mono-arrays (with some works, such as Ermakov et al. [17] and Abdulkadir et al. [18], further optimising layout based on site and dominant wave direction), the present work goes beyond power-based comparison to evaluate geometric efficiency (via the M-factor introduced in Section 2.2, which complements the H-factor of Zheng et al. [14]) and to examine the underlying hydrodynamic mechanisms, which previous works do not address in depth for arrays combining devices with different dominant DOFs.

Building upon Raghavan et al. 2025 [22], the present study extends the analysis to a substantially broader configuration space: 3360 cases spanning array sizes, spacings, layouts (rectangular and staggered), wave directions, and control strategies (active and passive) under both regular and irregular waves.

This paper systematically compares traditional mono-device WEC arrays with a new mixed array concept that combines different device types (specifically point absorbers and flaps) to exploit complementary dynamics. The paper begins explaining the framework (see Section 2 and Appendix) utilised for the hydrodynamic modelling of single WECs and WEC arrays used to evaluate 3360 distinct cases. It details the specific array configurations, including various sizes, layouts, and spacings, and defines the performance metrics, such as the interaction-based q-factor and the geometry-dependent M-factor. The results (see Section 3) are then presented through a comprehensive analysis of directional robustness, spacing sensitivity, optimal array identification and detailed explanations on the underlying hydrodynamics. The main discussion and conclusions are presented in Sections 4 and 5 respectively.

2. Materials and methods

A location off the north coast of the Netherlands was selected for this study. The Dutch coast offers several benefits for wave-energy deployment: (a) favourable coastal characteristics with smoother depth variation, (b) a significant resource of ≥7 kW/m available at shallow depths of 15 to 20 m, (c) high vessel accessibility due to milder mean conditions of ≥90%, (d) shared grid-connection hubs for accelerated proof-of-concept testing, and (e) smaller extreme waves reducing infrastructure costs.

Wave spectral data is taken from the ECHOWAVE [23] hindcast developed at the Marine Renewable Energies Lab (MREL). This 30 years high-resolution dataset was created using WW3 implemented with a

(a) Considered location at Lat 53.6°, Lon 6.3° off the coast of the Netherlands

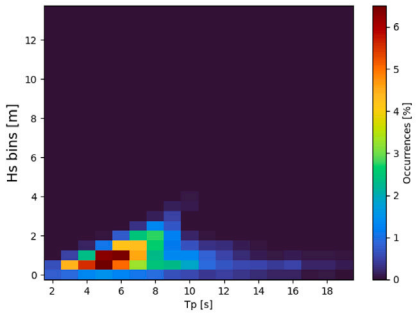

(b) Scatter diagram at Lat 53.6°, Lon 6.3° off the coast of the Netherlands

Fig. 1. Selected offshore location and corresponding wave climate off the coast of the Netherlands.

regular multi-grid 2-way nesting system, and adjustments specially aimed to improve its accuracy in Atlantic European coastal waters, which lead to the TUD-165 set of parameterisations. The wave spectrum is discretised in 36 directions and 36 exponentially spaced frequencies from 0.034 to 0.95 Hz, using a 1.1 increment factor from one frequency to the next. The maximum spatial resolution within the European coastal shelf is ~ 2.3 km.

The selected location at Lat 53.6°, Lon 6.3° lies 7.3 km off the coast of Schiermonnikoog (Fig. 1(a)). The site lies in a low- to mid-resource region, with peak occurrences at $H_s = 0.5$–1 m and $T_p = 5$ s (Fig. 1(b)), accounting for approximately 32% of occurrences. The dominant direction is not considered here, since the directional variation is one of the main aspects of this study.

A weakly non-linear frequency-domain framework based on HAMS-MREL is used for all hydrodynamic simulations. The model has been extensively validated [24] considering multiple WEC archetypes, rigid bodies with and without constraints with experimental data, semi-analytical solution in literature and cross-model comparison with BIEM commercial and open-source solvers such as WAMIT, NEMOH, Capytaine, as well as open-source CFD solvers such as OpenFOAM. The solver in HAMS-MREL has proven robust and offers parallelisation capacities, that significantly improve its computational efficiency.

The CorPower C4, originally designed for deep water [25], is used as the baseline PA. Two variants are derived from it (Table 1) to study size effects in mixed arrays, not as alternative references: a smaller PA (6 m diameter) for improved wavelength-to-diameter scaling, reduced orbital-velocity variation, and greater seabed clearance in shallow water; and a larger PA (12 m diameter, natural period ≈ 4.5 s) tuned closer to the site's peak period. The diameter-to-draft ratios differ from the C4 because the draft is limited by the shallow-water depth, while the diameter is varied to meet these hydrodynamic objectives. The flap device properties are taken from [26] and given in Table 2.

For the flap, viscous effects are significant; neglecting them can lead to absorbed power differences of up to 33% for $T_p = 8$–15 s at $H_s = 1.5$ m, and up to 100% at higher H_s [27]. For the PA, viscous effects are moderate in the present shallow-water study ($H_s \leq 2$–2.5 m), though including viscous drag improves prediction accuracy and robustness by partially compensating for unmodelled nonlinear Froude–Krylov (NLFK) effects [28]. Non-linear hydrostatic and NLFK effects can matter for near-hemispherical PAs in moderate to high seas [29]; however, the low sea states considered here and the displacement limit when considering active control of 1.2 m (≈30% of draft) restrict submerged area variation to 7%–9%, justifying their omission. A taut mooring system is assumed but not explicitly modelled, as previous work shows minimal influence on heave response at 15 m depth [30,31].

A weakly non-linear modelling framework was utilised based on BIEM (described in detail in Appendix). Convergence studies were performed for all meshes. The minimum panel size was estimated as $\lambda/6$ [11], yielding 2.34 m at $T = 3$ s and 14.5 m depth. While a mesh sufficient for a single device is generally adequate for multiple devices [32], higher-resolution meshes were adopted to better capture interaction effects at narrower spacings [33]: 715 panels (small PA), 724 panels (large PA), and 1074 panels (flap hull and foundation). A waterplane mesh was used for the PA to suppress irregular frequencies. Computation time in HAMS-MREL scales approximately with N_p^3 [24]. The final meshes are shown in Fig. 2.

Table 1
Properties of the PA devices.

(a) Small PA device			(b) Large PA device		
Property	Value	Unit	Property	Value	Unit
Diameter	6	m	Diameter	12	m
Weight	70	T	Weight	272	T
Draft	4	m	Draft	4	m

Table 2
Properties of the flap device.

Property	Value	Unit
Width	17.7	m
Height	10.6	m
Peak thickness (at 7.1 m from bottom)	3	m
Moment of inertia	8.8×10^6	kg m^2
Draft	9	m

The natural periods of the small and large PA are 3.6 s and 4.5 s, respectively, and that of the flap is 17.5 s. Detailed derivations for natural frequencies, equations of motion, array implementation (mixed and mono), and the active and passive control strategies are presented in Appendix.

2.1. Considered configurations

Two sets of arrays are considered: one combining the small PA with the flap, and the other the large PA with the flap. For each set, three array types are analysed—PA-only, flap-only, and mixed PA-flap–following a consistent geometric logic. Arrays of 2, 4, 7, and 10 devices are examined. For arrays with four or more devices, both rectangular (regular grid) and staggered (half-spacing offset, diamond-like packing) layouts are considered. All arrays are evaluated at four normalised spacings of $4C$, $6C$, $8C$, and $10C$, where C is the characteristic device dimension (diameter D for the PA, width W for the flap, and an averaged dimension for mixed arrays), enabling investigation of near-field to far-field hydrodynamic interactions.

Each array is subjected to 12 incident-wave directions at 30° intervals covering the full 360° range. For flap devices, 0° corresponds to broadside incidence (perpendicular to the flap length), which is hydrodynamically significant due to the strongly direction-dependent excitation and radiation patterns of flaps. PAs are axisymmetric in

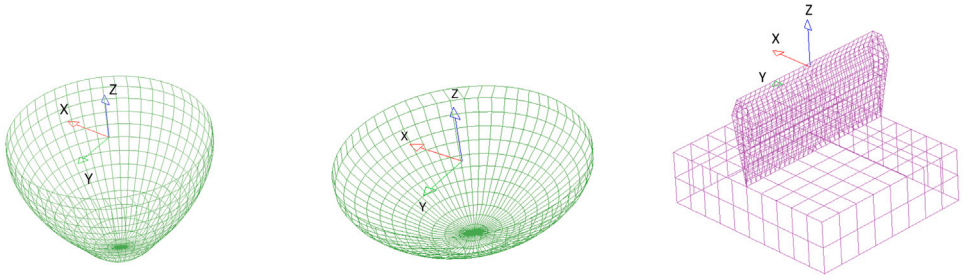

(a) Small PA (715 panels) (b) Large PA (724 panels) (c) Flap (1074 panels)

Fig. 2. Meshes for the three WEC devices.

heave and thus directionally insensitive in isolation, though array interactions introduce directional variability. Mixed arrays combine these characteristics, often producing more asymmetric and, in some cases, more constructive interaction patterns than mono arrays.

The array sizes span from the simplest pairwise interaction scenario (2 devices) to elongated multi-row arrays (10 devices) where long-range diffraction and radiation effects become pronounced. Considering all variations, a total of $(3\times4\times12\times2+4\times12)\times2=672$ cases per array type are evaluated under both passive and active control, yielding 3360 cases across all five array types.

All the array configurations are shown from Figs. 3(a) to 3(c).

2.2. Metrics for comparing mixed and mono arrays

To analyse array performance under both regular and irregular waves, three metrics are considered: the q-factor, which quantifies hydrodynamic interaction effects; the H-factor of Zheng et al. [14], which compares total absorbed power in hybrid arrays against their mono equivalents; and the M-factor introduced by Raghavan et al. [34], which extends this comparison to per-unit-width capture efficiency. The final analysis focuses on the q-factor and the M-factor, which together capture interaction-driven behaviour and geometry-normalised efficiency, with the H-factor referenced as the established precedent for hybrid-array power balance.

The q-factor is the ratio of array power to isolated-device power, indicating whether a configuration is destructive ($q<1$) or constructive ($q>1$):

$$q=\frac{P_{arr}}{m\cdot P_p+n\cdot P_f}, \tag{1}$$

where m and n are the number of PAs and flaps, and P_p, P_f their respective isolated powers. For the flap, the isolated-device power is taken in the most favourable direction (0° or 180°).

For mixed-array configurations, the H-factor of Zheng et al. [14] compares the total absorbed power of the mixed array against the count-weighted sum of the total powers of the two equivalent-size mono-type arrays:

$$H=\frac{P_{mixed}}{\frac{m}{m+n}P_{p,\mathrm{mono}}+\frac{n}{m+n}P_{f,\mathrm{mono}}}, \tag{2}$$

where $P_{p,\mathrm{mono}}$ and $P_{f,\mathrm{mono}}$ are the total powers of $(m+n)$-device PA-only and flap-only mono farms, respectively. Substituting the CWR-to-power identity $P=(mD+nW)\,\eta\,P_{inc}$ for the hybrid farm and the corresponding identities for the two mono farms, the H-factor can equivalently be written as

$$H=\frac{(mD+nW)\,\eta_{mixed}}{mD\,\eta_p+nW\,\eta_f}. \tag{3}$$

Eqs. (2) and (3) are algebraically equivalent: the apparent width-like coefficients mD and nW in Eq. (3) arise from the algebraic translation between power and CWR and reflect the underlying power-level comparison, rather than constituting a separate weighting choice on the

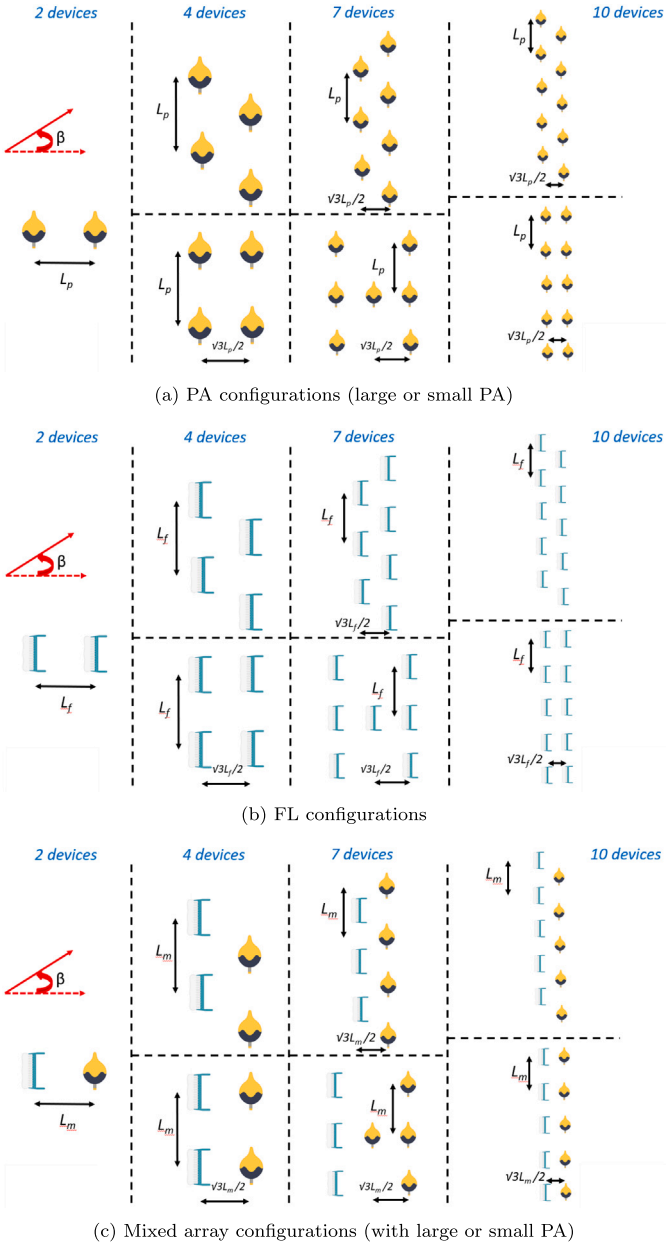

(a) PA configurations (large or small PA)

(b) FL configurations

(c) Mixed array configurations (with large or small PA)

Fig. 3. Array configurations considered in this study: (a) PA arrays, (b) FL arrays, and (c) mixed arrays.

CWRs themselves. The H-factor is therefore most naturally understood as a power-balance metric, indicating whether mixing produces more or less total power than a device-share-weighted sum of the equivalent mono farms. This is informative for absolute output, but does not account for differences in the characteristic dimensions, and thus the intercepted wavefront, of the devices involved. This limitation can be significant for the configurations examined here: in the small PA–flap array, for example, the PA has a diameter of 6 m while the flap has a width of 17.7 m. Under such disparities, two configurations can return similar H-factor values (particularly under active control where the ratio of powers produced by the two device classes can be as small as 1 : 2 for PA:flap) while differing substantially in how efficiently each device converts the wavefront it actually intercepts. Zheng et al. [14] also propose a capacity-factor-based reformulation along similar lines, but it remains anchored to overall array power rather than to the geometric disparity between devices, and therefore does not serve the same purpose.

The M-factor (Mixed factor), introduced by Raghavan et al. [34], addresses this geometric limitation by performing the comparison directly at the level of capture-width ratios (CWRs), with no intermediate step through total power:

$$M = \frac{\eta_{mixed}}{\left(\frac{m}{m+n}\eta_p + \frac{n}{m+n}\eta_f\right)}, \tag{4}$$

where the capture-width ratios are

$$\eta_{mixed} = \frac{P_{mixed}}{(m \cdot D + n \cdot W) \cdot P_{inc}}, \qquad \eta_p = \frac{q_p \cdot P_p}{D \cdot P_{inc}}, \qquad \eta_f = \frac{q_f \cdot P_f}{W \cdot P_{inc}}, \tag{5}$$

with D the PA diameter, W the flap width, P_{inc} the incident wave power (kW/m), and q_p, q_f the q-factors of the PA-only and flap-only mono arrays of equivalent total size (m+n). By comparing the CWR of the mixed array against the count-weighted average of the CWRs of its constituent mono arrays, the M-factor places all configurations on a common per-unit-width basis: $M > 1$ indicates that the mixed array absorbs more power per unit intercepted wavefront than the equivalent mono configurations, while $M < 1$ indicates that it absorbs less. This distinction is particularly relevant for the site-selection (shallow or deep water) and layout decisions considered in this work, since the same WEC type deployed in different depth conditions may require different sizes, which the M-factor accounts for through its geometric normalisation.

The M-factor and H-factor are structurally distinct rather than cosmetic variants of one another. Equating the denominators of Eqs. (3) and (4) requires the count-based weights $m/(m+n)$, $n/(m+n)$ to coincide with the width-derived coefficients $mD/(mD+nW)$, $nW/(mD+nW)$, which holds if and only if $D = W$. For the mixed PA/flap arrays considered here the geometric ratios are $W/D \approx 3$ for the small PA–flap array and $W/D \approx 1.5$ for the large PA–flap array, so the two metrics give meaningfully different readings and can in fact yield opposite verdicts (constructive versus neutral mixing) for the same configuration. The two are therefore treated as complementary in this work: the H-factor addresses the question of whether the mixed array produces more total power than its mono equivalents, and the M-factor addresses the question of how efficiently the mixed array converts the wavefront it intercepts on a per-unit-width basis. The latter question is particularly pertinent in the techno-economic framing of mixed PA/flap arrays, where CAPEX and OPEX scale per device rather than per metre of frontage, and a geometrically more efficient device class can help drive these costs down further.

The q-factor and the M-factor together capture complementary aspects of array performance: the q-factor measures absorbed power relative to isolated devices and quantifies the strength of hydrodynamic interactions, while the M-factor measures absorbed power per unit characteristic device width and quantifies geometric efficiency. As a purely hydrodynamic metric, the M-factor complements rather than replaces economic metrics such as LCOE or capacity factor: it isolates hydrodynamic efficiency from cost assumptions and translates directly into annual energy production (AEP), which feeds into both LCOE and capacity-factor calculations downstream. For these reasons, the final analysis in this work focuses on the q-factor and the M-factor, with the H-factor reported alongside where directly comparable for context.

3. Results

The isolated single devices are first analysed. The absorbed power from the small PA under active and passive control in regular waves (Fig. 4(a)) and irregular waves (Fig. 4(b)) is shown. Active control yields approximately 4.5 times higher peak power in regular waves owing to enforced phase alignment, narrowing near the PA's natural period (3.6 s) where both strategies approach resonance. In irregular waves, this ratio increases to nearly eight times due to the spectral-domain viscous damping formulation and energy-period PTO tuning. A similar behaviour is observed for the larger PA (Figs. 4(c) and 4(d)).

The flap device power (Figs. 4(e) and 4(f)) shows that, unlike the PA, the two control strategies do not converge near the flap's natural period (17.5 s) due to the displacement constraint in active control. Under passive control, the small PA produces approximately 1/10th the flap's power (1/4th for the large PA); under active control these ratios improve to 1/5th and 1/2 respectively, demonstrating greater benefits of active control for PAs than for flaps. These differences are reflected in the array results discussed later.

3.1. Comparing mean q-factor across all configurations and directions

One of the most common metrics is the q-factor, see Eq. (1). Fig. 5 shows the mean q-factor variation over the 3–12 s period range across all configurations (directions, array sizes, spacings) for the active control strategy under regular and irregular waves. For brevity, the behaviour considering passive control is only explained in the text. This period band corresponds to the dominant sea states at $H_s = 1$ m.

Mono PA arrays generally remain clustered near unity with narrow spread, indicating robust, directionally insensitive interactions. Mono flap arrays exhibit the widest spread, from fully destructive ($q = 0$) at perpendicular incidence (90°, 270°) to almost constructive values. Mixed arrays display intermediate behaviour, with the broadest performance envelope under active control (peak mean q-factor of 1.22 under active control and 1.19 under passive control). Increasing PA size shifts the mixed-array envelope upward to a higher bound, an effect most pronounced in irregular seas under active control, where the larger PA raises both the lower bound and constructive ceiling while reducing susceptibility to destructive interactions.

The directional dependence of the mean q-factor is explicitly examined for all arrays. Consistent patterns emerge: mono PA arrays are the most directionally robust ($q \approx 1$), mono flap arrays collapse to $q = 0$ near 90° and 270°, and mixed arrays consistently outperform mono flaps at all directions, maintaining non-zero q-factors even at perpendicular incidence. Increasing PA size produces a systematic upward shift across the full directional range.

Only the results with active control are shown here for brevity. The behaviour under passive control is explained.

Under passive control, mixed-array performance lies between mono PA and mono flap, with pronounced but not fully destructive reductions near 90° and 270°. Irregular seas show reduced directional contrast due to spectral averaging; PA size plays a particularly prominent role in stabilising performance, with large-PA minimum q-factors significantly exceeding those of the small PA.

Under active control (see Fig. 6), mixed arrays benefit most, outperforming both mono configurations—particularly around 0° and 180°. With the large PA, mixed arrays achieve the highest mean q-factors in the directional analysis of 1.22. A consistent asymmetry is observed, with higher performance at 180° where PAs encounter the

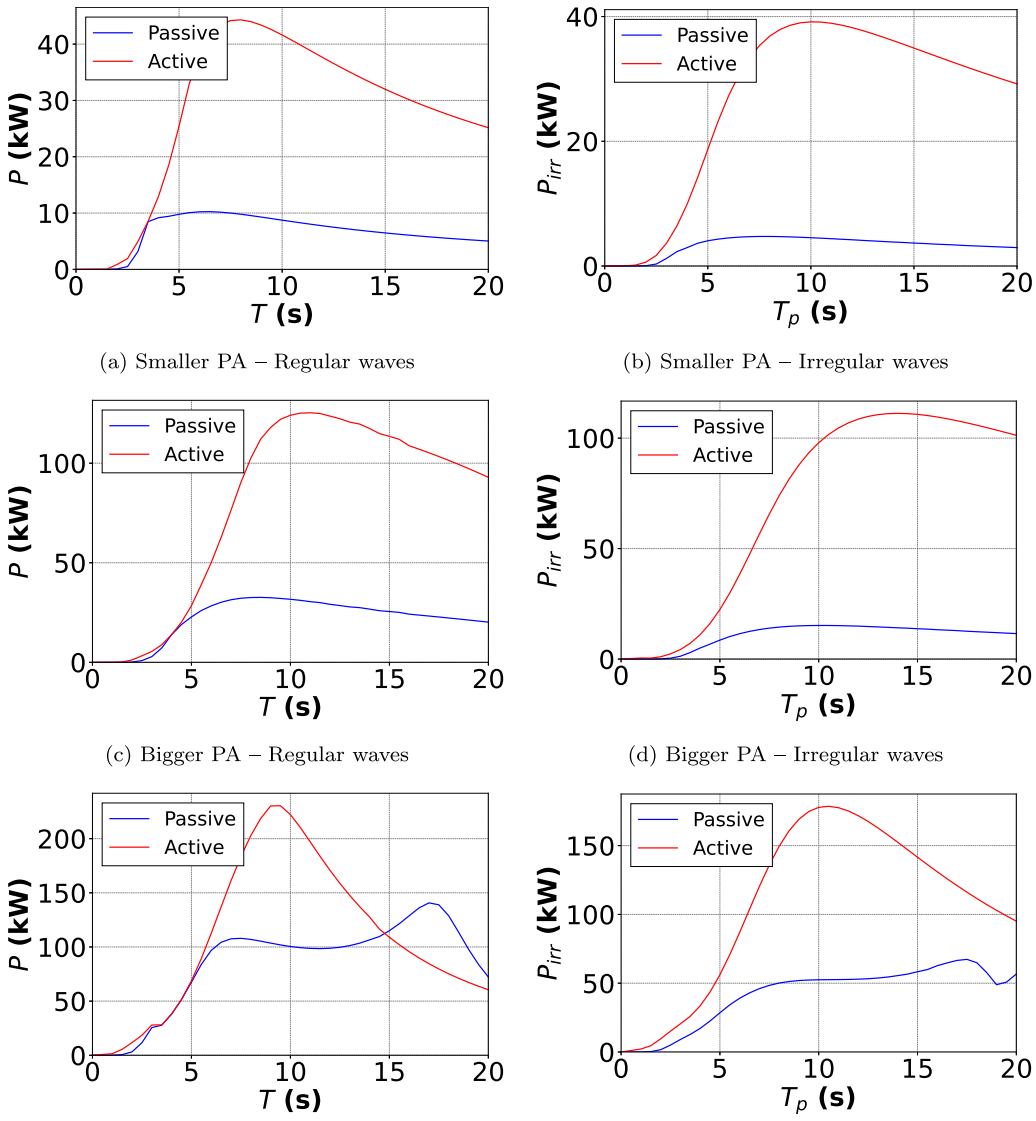

(a) Smaller PA – Regular waves

(b) Smaller PA – Irregular waves

(c) Bigger PA – Regular waves

(d) Bigger PA – Irregular waves

(e) Flap – Regular waves

(f) Flap – Irregular waves

Fig. 4. Single device power output for each WEC type under regular (left) and irregular (right) wave conditions.

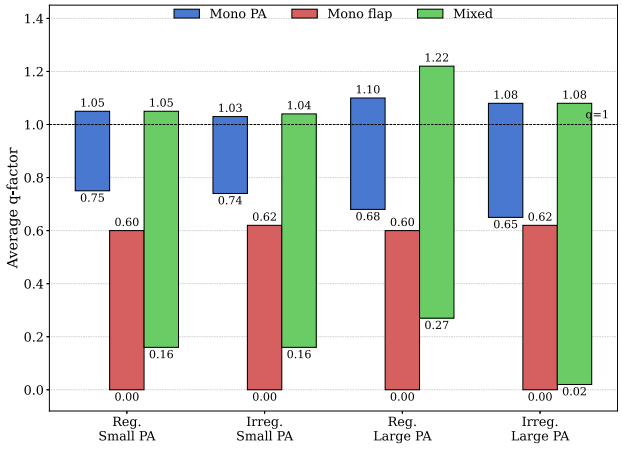

Fig. 5. Average q-factor range (min–max) across wave incidence angles for mono PA, mono flap, and mixed array configurations under active control.

incident wave first and induce less severe wave-field distortion before interacting with downstream flaps.

Fig. 7 presents the average M-factor range across wave directions for irregular waves for active control (The irregular waves considering passive control and the regular wave cases is not shown for brevity, but is explained here).

When considering regular waves, both device combinations exhibit strong directional dependence, with the highest values at head-on incidence (0°, 180°) and the lowest at beam seas (90°, 270°). The smaller combination achieves higher peak M-factors (exceeding 1.75 under passive control at head-on directions) but suffers greater degradation at beam seas ($M < 0.6$). The bigger combination displays a more uniform directional response, remaining above 0.79 even at beam seas, though active control introduces wider M-factor ranges at certain oblique directions (60°, 240°).

Under irregular waves, directional trends are broadly consistent but with reduced magnitudes due to spectral averaging. A notable finding under active control for the bigger PA-flap combination is that certain configurations at 60°, 240°, and 300° yield near-zero M-factors, highlighting the importance of careful layout optimisation when deploying larger mixed arrays with active control.

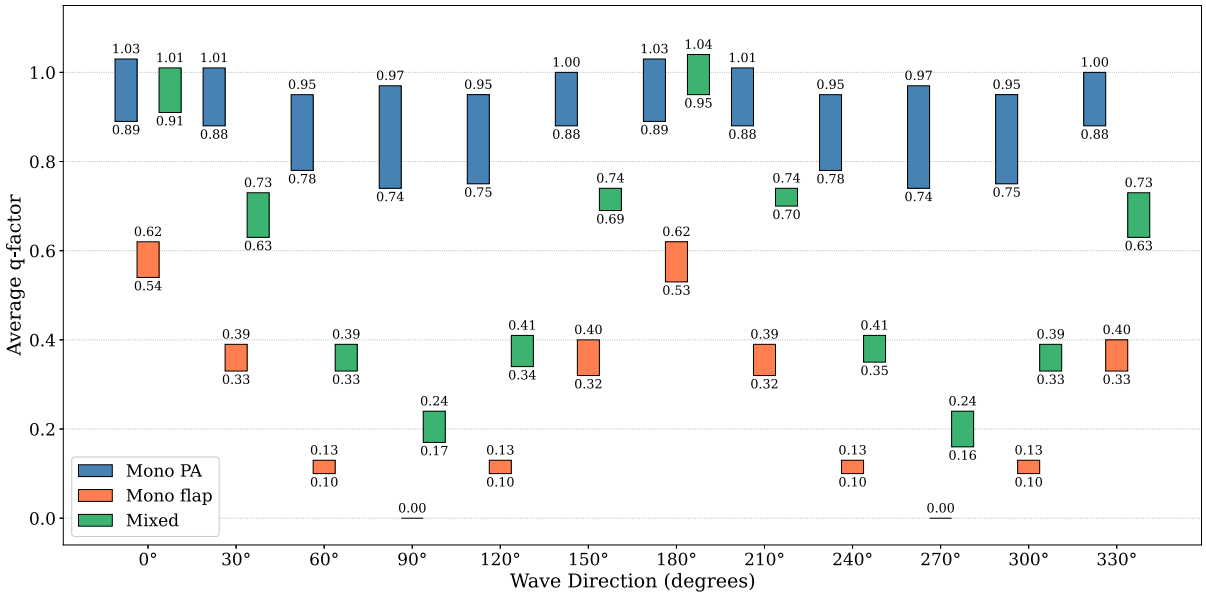

(a) Small PA

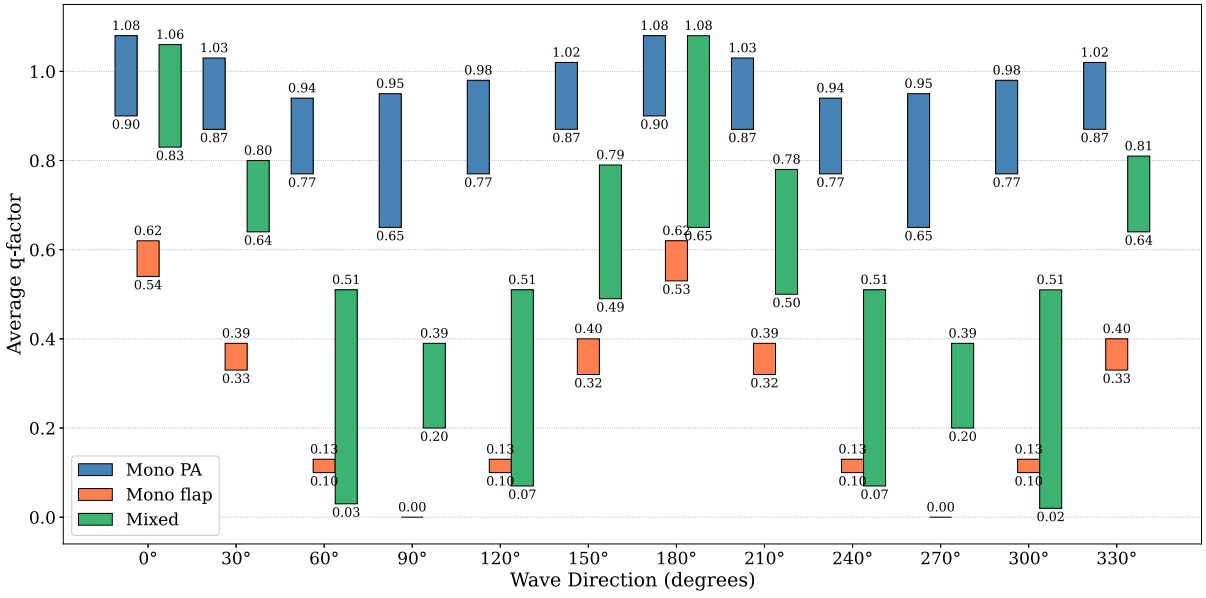

(b) Large PA

Fig. 6. Directional comparison of mono and mixed arrays under irregular waves and active control.

3.2. Variation of mean q-factor with WEC number variation

This section examines how the mean q-factor (averaged over T = 3–12 s) varies with number of devices (only active irregular cases shown for brevity, Fig. 8). For two-device arrays, rectangular and staggered layouts are geometrically equivalent.

Mono PA arrays exhibit q-factors close to unity for aligned headings, with reductions for oblique directions that intensify with array size at tight spacings ($4D$). Staggered layouts outperform rectangular ones at small spacings. Large PAs show stronger scaling effects due to their larger hydrodynamic footprint. Mono flap arrays are dominated by directional excitation, with transverse incidence yielding near-zero q-factors regardless of configuration.

Mixed arrays moderate the dependence on array size, with q-factors remaining non-zero for all directions. The PA component provides a stabilising baseline while the flap contributes at aligned headings. Intermediate spacings ($6D$–$8D$) offer the best compromise. Active control improves robustness for all array types, enabling the highest constructive q-factors for mixed arrays with large PAs at aligned headings. Small-PA mixed arrays provide the most consistent performance, while large-PA mixed arrays achieve higher peaks at the cost of broader directional spread. A consistent asymmetry between 0° and 180° is observed, with higher performance at 180° where PAs encounter the incident wave first.

3.3. Variation of mean q-factor with WEC spacing

This section examines how the mean q-factor varies with inter-device spacing from $4D$ to $10D$ (only active irregular cases shown for brevity, Fig. 9). Representative array sizes are shown; behaviour for other sizes is qualitatively similar.

For mono PA arrays, tight spacing ($4D$) produces the strongest interaction effects, while increasing spacing towards $10D$ progressively

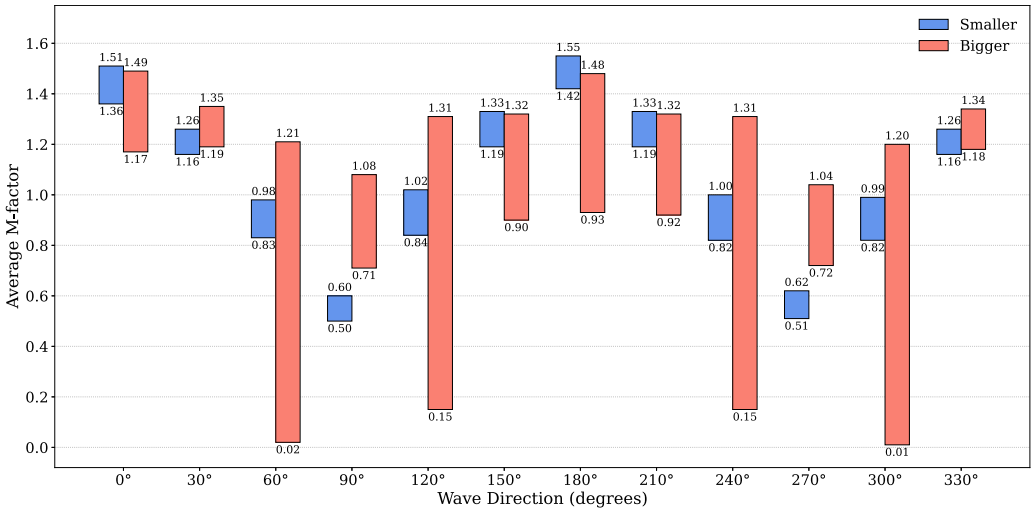

Fig. 7. M-factor range by wave direction for mixed WEC arrays under irregular waves with active control, comparing smaller and bigger device combinations.

weakens coupling. Staggered layouts outperform rectangular ones at small spacings. Large PAs exhibit stronger spacing sensitivity, yielding higher constructive gains at $6D$–$8D$ for aligned incidence but deeper interaction troughs at $4D$. Mono flap arrays are largely insensitive to spacing, with performance governed by directional excitation.

Mixed arrays show moderate spacing dependence balancing PA-driven interactions and flap directional selectivity. At $4C$, the largest off-axis penalties occur; intermediate spacings ($6C$–$8C$) typically improve performance; by $10C$, q-factors cluster near unity. Active control accelerates convergence towards isolated behaviour with spacing. Small-PA mixed arrays provide the smoothest behaviour across $4C$–$10C$, while large-PA mixed arrays offer higher peaks at intermediate spacings but display stronger sensitivity at $4C$. Both configurations approach comparable performance by $10C$.

3.4. Variation of mean M-factors with number of devices and spacing

This section examines mean M-factor variation with number of devices and spacing for mixed arrays (only active control irregular wave cases shown for brevity, Fig. 10).

The mean M-factor is primarily governed by wave direction. Aligned headings (0°, 180°) consistently yield M well above unity, typically increasing from $N_b = 2$ to intermediate arrays before saturating; 180° generally outperforms 0°, suggesting PA-radiated fields benefit downstream flaps more than vice versa. Moderately oblique directions maintain $M > 1$ with limited sensitivity to array growth, while transverse directions (90°, 270°) produce the lowest M-factors.

Small-PA mixed arrays display stable behaviour across array sizes ($M \approx 1.1$–1.3 under irregular active control), whereas large-PA arrays exhibit more pronounced variations with N_b due to stronger cumulative radiation effects but can reach higher peak efficiencies. Mixed configurations maintain $M > 1$ across the full spacing range ($4C$–$10C$), with spacing playing a secondary role to direction. Small-PA arrays show the greatest spacing insensitivity, while large-PA arrays display shallow maxima at intermediate separations under passive control and highest values at tight spacings under active control. Overall, both mixed configurations avoid the severe efficiency collapse of mono-flap arrays, with small-PA arrays providing greater robustness and large-PA arrays delivering higher peak efficiencies.

3.5. Optimal WEC array identification

While q-factors quantify performance relative to isolated devices, M-factors normalise power based on the distinct physical dimensions of PAs and flaps, providing a clearer comparison of hydrodynamic efficiency across array types. Only Fig. 11 for optimal configuration in irregular waves is shown for brevity, the same is followed for the regular waves.

Under regular waves, the 10-device staggered mixed array (5 large PAs + 5 flaps) with active control is identified as the best overall configuration, achieving the highest mean M-factor and thus superior capture-width efficiency. Under irregular waves, the same 10-device staggered mixed array remains preferred, in this case with passive control. Although configurations such as the 4 PA + 3 flap array may yield slightly higher q-factors for specific headings, the 10-device large-PA array achieves the highest mean M-factor and consistently outperforms mono arrays.

The following sections provide further insights into this 10-device staggered configuration (5 large PAs + 5 flaps, see Fig. 3(c)) under regular and irregular waves.

3.6. WEC array regular wave hydrodynamics

The optimal regular wave configuration is the 10-device array (5 large PAs + 5 flaps, $L_m = 10C$, $C = 15$ m) with active control, achieving mean $q > 1$ at 0° and 180° and mean $M > 1$ for all directions except 90° and 270°. To explain the hydrodynamics further, the 0° direction is selected with two contrasting periods: $T = 6$ s (best mixed-array performance, $q = 1.6$, $M = 2.25$) and $T = 6.5$ s (worst performance relative to mono arrays), as shown in Fig. 12.

Table 3 presents percent changes in key hydrodynamic parameters for mixed-array devices relative to their mono-array counterparts, while Table 4 summarises the radiation damping cross-coupling, which exhibits a critical sign reversal between the two periods.

At $T = 6.0$ s, the mixed array benefits from favourable interactions across both device types. Flap excitation forces increase by 34% relative to the mono flap array due to beneficial wave scattering from neighbouring PAs. Radiation damping cross-coupling is predominantly positive ($+6.43 \times 10^6$ Ns for PA→flap; 32 positive vs. 18 negative elements, see Fig. 13), indicating that radiated waves reinforce adjacent device motion. PAs exhibit an 11% reduction in added mass, shifting their response closer to resonance, while active control increases PTO damping for both PAs (6.2%) and flaps (10.9%). Collectively, these effects produce a 175% increase in PA heave RAO, while the flap pitch RAO remains relatively unchanged (−7%; see Table 3). It is important to reiterate that since the devices operate under active control, they are subjected to displacement constraint and the increments observed in the response also considers this.

At $T = 6.5$ s, the interactions become unfavourable. Excitation forces decrease by 24% (PA) and 16% (flap), while radiation damping

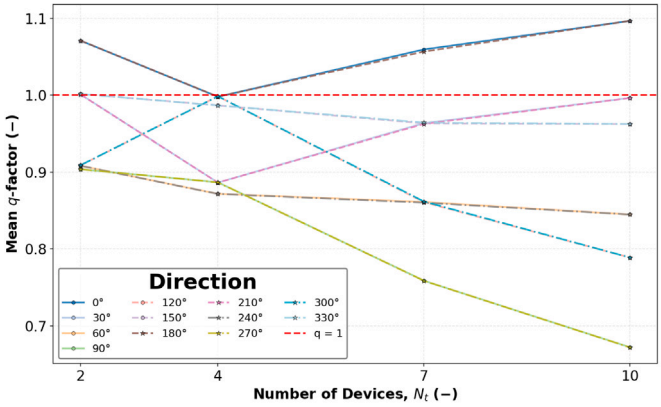

(a) Big PA mono: $4D$, staggered

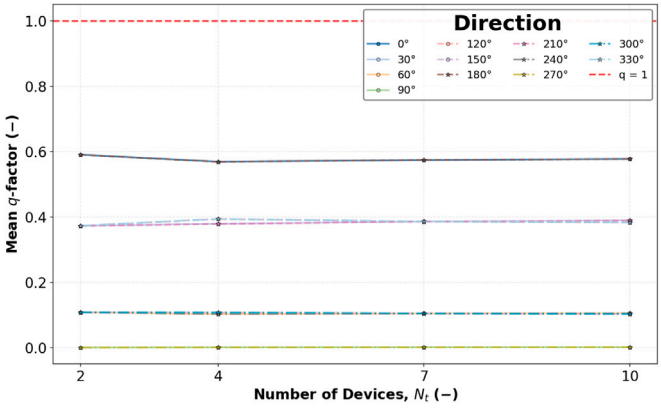

(b) Flap mono: $6D$, staggered

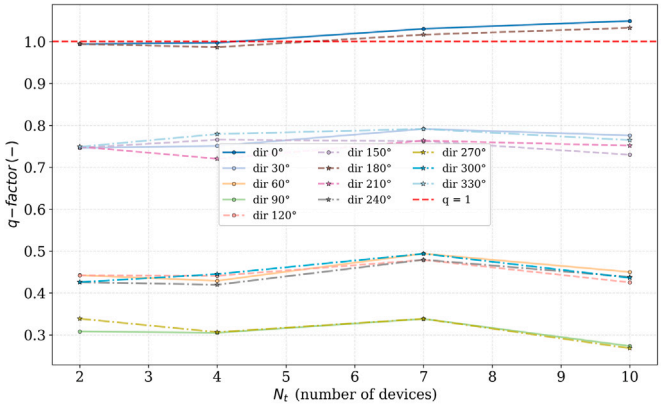

(c) Mixed (big PA + flap): $8D$, staggered

Fig. 8. Mean q-factor vs. number of devices under irregular waves, active control.

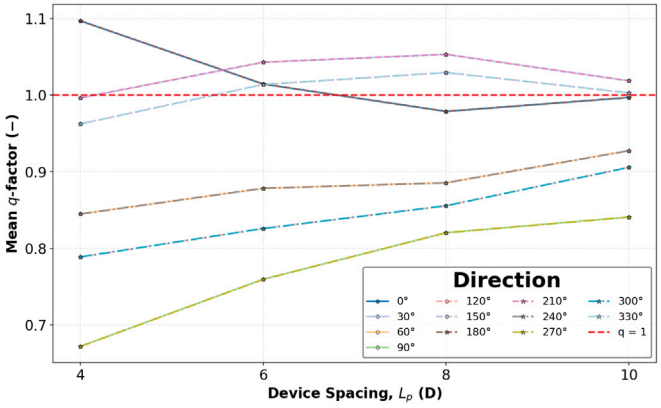

(a) Big PA mono: $N_b = 10$

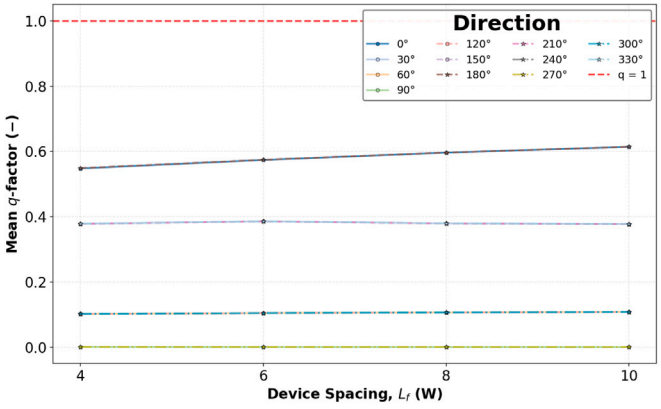

(b) Flap mono: $N_b = 7$

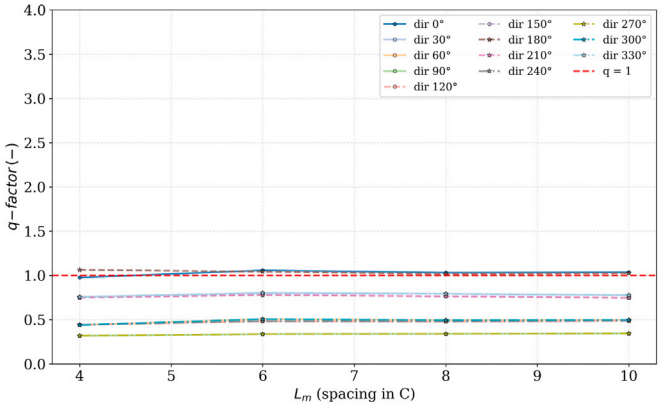

(c) Mixed (big PA + flap): $N_b = 7$

Fig. 9. Mean q-factor vs. spacing under irregular waves, active control (staggered layouts).

cross-coupling reverses sign to predominantly negative (see Fig. 13), opposing device motion. The most severe consequence is a 55% reduction in flap pitch RAO, which dominates the overall performance deterioration.

The free-surface disturbance coefficient $K_d = |\eta_{\text{total}}|/|\eta_{\text{inc}}|$ (Fig. 14) further elucidates these differences. At $T = 6$ s (Fig. 14(a)), the mixed array shows pronounced amplification in front of PAs (K_d up to 2.1) and near flaps (up to 1.8), while PA mono arrays display the weakest amplification ($K_d \approx 1.2$). At $T = 6.5$ s (Fig. 14(b)), mono flap arrays dominate with K_d up to 2.7, while mixed arrays behave more similarly to PA mono arrays with limited interaction.

This performance contrast is explained by the spacing-to-wavelength ratio. At $h = 14.5$ m, $\lambda_w = 52.8$ m for $T = 6.0$ s and $\lambda_w = 60.0$ m for $T = 6.5$ s. At $T = 6.0$ s, the mixed array spacing approaches a near-integer multiple ($L_m = 2.84\lambda_w \approx 3\lambda_w$), favouring constructive interference, whereas both mono arrays deviate from integer multiples. At $T = 6.5$ s, the mono array spacings correspond to exact integer multiples ($L_f = 3.00\lambda_w$, $L_p = 2.00\lambda_w$), promoting constructive interference, while the mixed array spacing ($L_m = 2.50\lambda_w$) represents a half-integer multiple, inducing destructive interference.

The diffraction and radiation percentage plots (Figs. 15 and 16) corroborate these findings. At $T = 6$ s, PA mono arrays are diffraction-dominated with localised radiation, while in the mixed array the flap

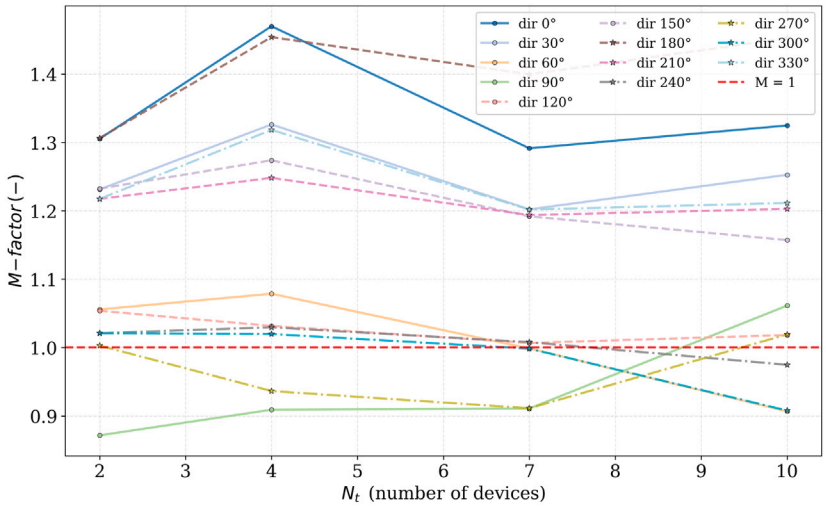

(a) Big PA–flap: $4C$, vs. N_b

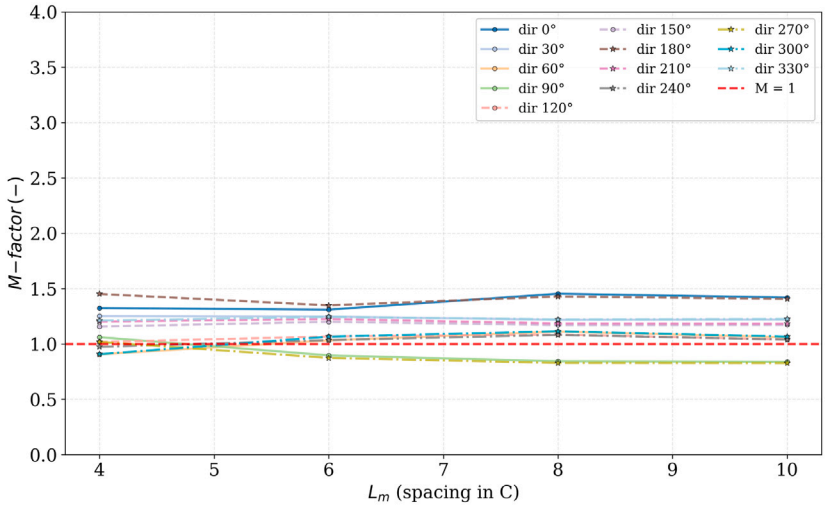

(b) Big PA–flap: $N_b = 10$, vs. spacing

Fig. 10. Mean M-factor vs. number of devices and spacing under irregular waves, active control (staggered layouts) for mixed arrays with Big PA.

Table 3
Percent changes in hydrodynamic parameters: Mixed array vs. Mono arrays. Positive values indicate an increase in the mixed array; negative values indicate a decrease.

Parameter	$T = 6.0$ s		$T = 6.5$ s	
	PA	Flap	PA	Flap
Excitation force	+2.6%	**+34.1%**	**−23.6%**	**−15.6%**
Added mass (diagonal)	−11.4%	+11.2%	−0.1%	−5.3%
Radiation damping (diagonal)	+5.5%	+17.1%	−10.4%	+5.7%
PTO damping (real part)	+6.2%	+10.9%	+0.0%	−5.3%
RAO	**+174.9%**	−7.3%	+34.8%	**−55.2%**

Table 4
Radiation damping cross-coupling in the mixed array at $T = 6.0$ s and $T = 6.5$ s.

Parameter	$T = 6.0$ s	$T = 6.5$ s
PA→Flap sum	$+6.43 \times 10^6$ Ns	-2.08×10^6 Ns
Flap→PA sum	$+5.65 \times 10^6$ Ns	-3.45×10^6 Ns
Sign distribution	32 pos, 18 neg	11 pos, 39 neg
Interaction type	**Constructive**	**Destructive**

radiation fields interact constructively with those of the PAs. At $T = 6.5$ s, flap mono arrays clearly dominate with significantly stronger and more spatially extended radiation fields, consistent with their enhanced constructive interference at this period.

3.7. WEC array irregular wave hydrodynamics

The 10-device staggered configuration (5 PAs + 5 flaps) with $4C$ spacing under passive control was identified as the best irregular-wave configuration, giving a mean q-factor of 1.19 and mean M-factor of 1.4 across 3–12 s, with $M > 1$ for 10 of 12 directions.

At head-on incidence (0°, Fig. 17(a)), the mixed array consistently outperforms both mono configurations, achieving a maximum q-factor of approximately 1.2 with M-factors consistently above unity. The PA mono array shows modest enhancements (q slightly above unity for $T_p \approx 3$–6 s), while the flap mono array exhibits weaker trends with q near unity. The clear separation between mixed and mono array metrics highlights favourable PA–flap coupling under head-on conditions.

At 90° (Fig. 17(b)), all configurations exhibit $q < 1$. The flap mono array produces negligible power due to perpendicular wave incidence, while the mixed array shows only limited improvement, confirming that without favourable directional alignment, hydrodynamic coupling becomes predominantly destructive.

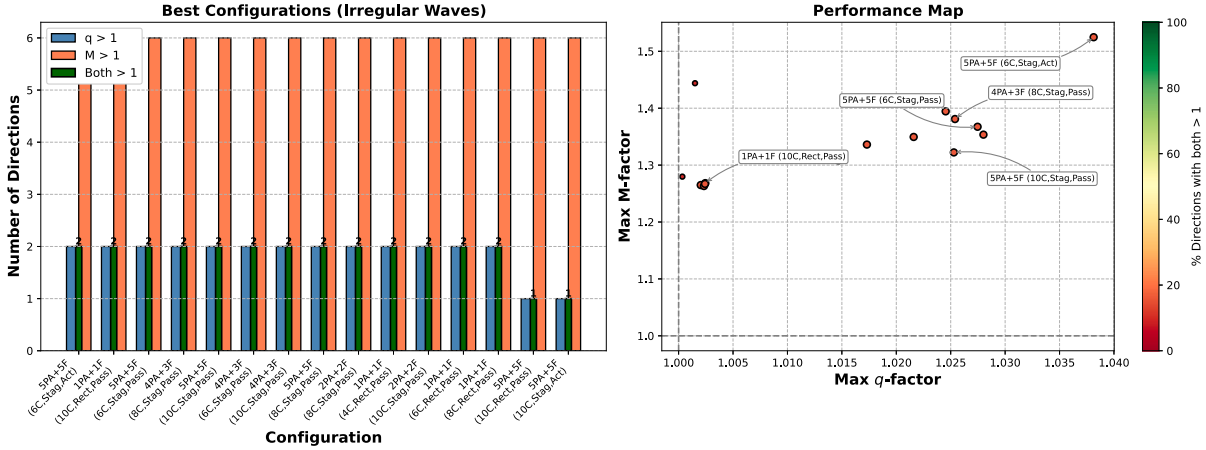

(a) Small PA + flap

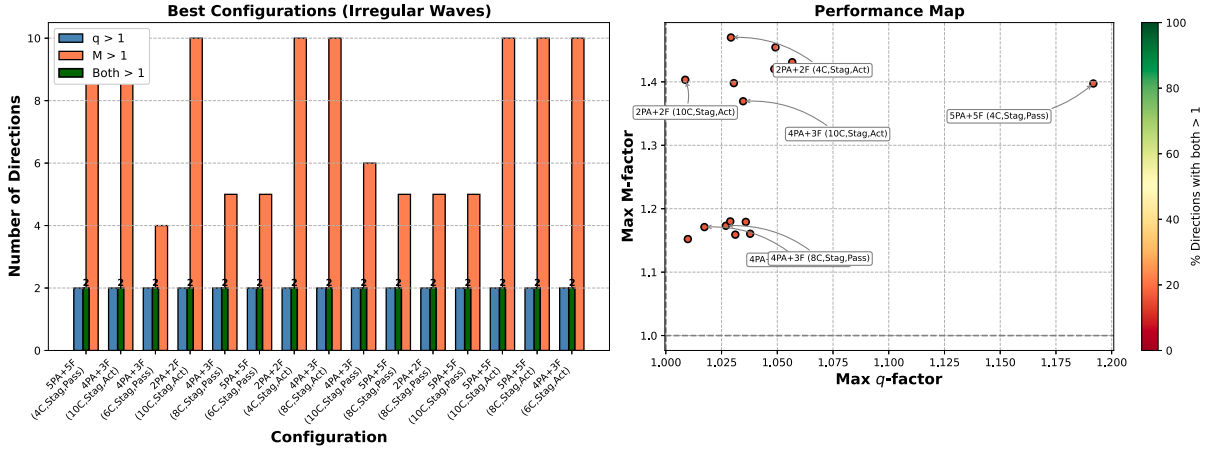

(b) Big PA + flap

Fig. 11. Best-performing mixed array configurations under irregular wave conditions.

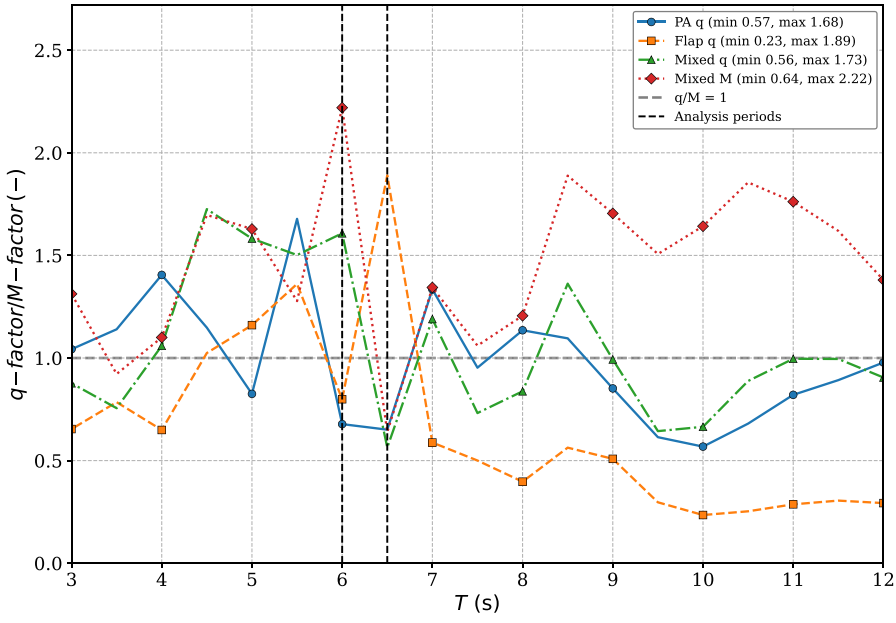

Fig. 12. q and M-factor for the mono and mixed arrays with two analysis periods of $T = 6$ and 6.5 s.

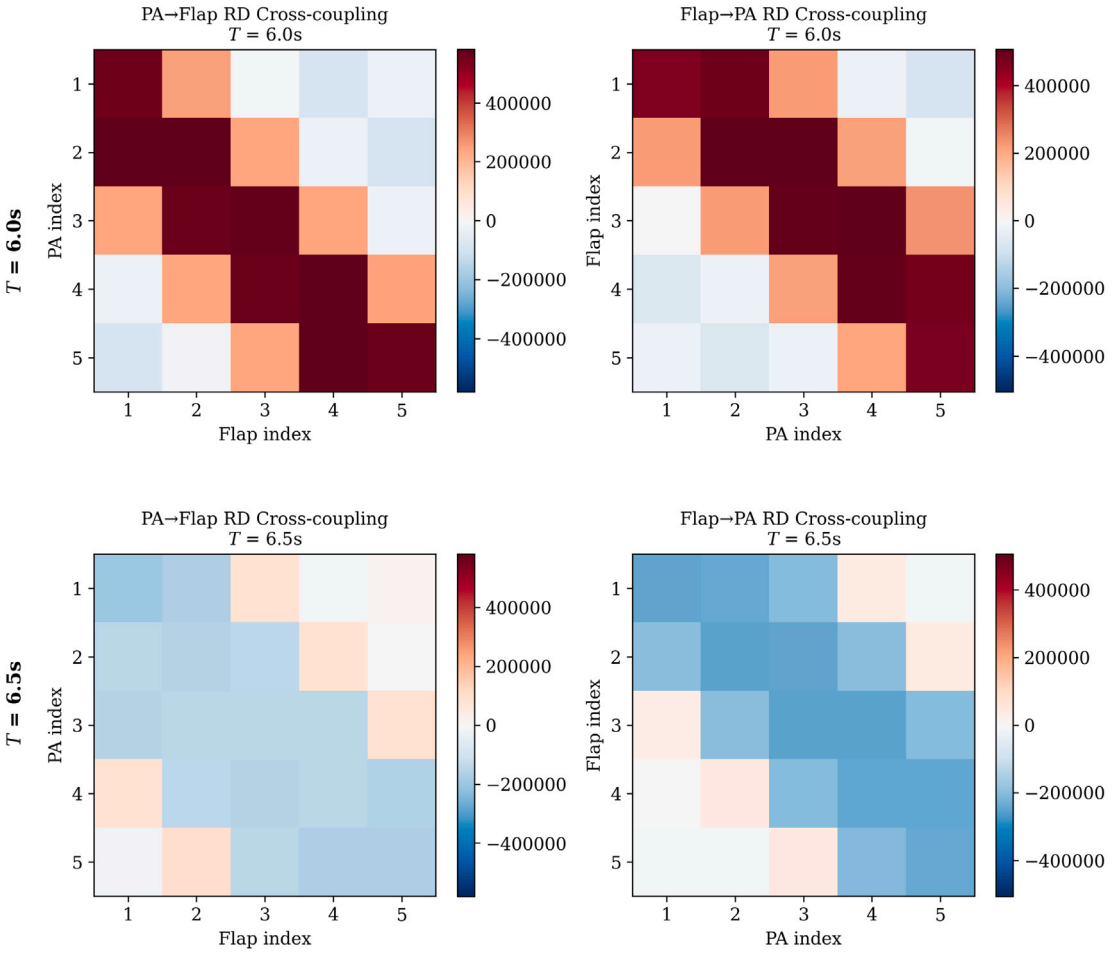

Fig. 13. Radiation damping cross-coupling matrices between PA and flap devices in the mixed array. All units are in Ns. Top row: $T = 6.0$ s showing predominantly positive (red) values indicating constructive interaction. Bottom row: $T = 6.5$ s showing predominantly negative (blue) values indicating destructive interference.

Individual device power at 0° (Fig. 18) confirms these trends. In the PA mono array (Fig. 18(a)), arrayed PAs closely follow the isolated response with slight enhancements for $T_p \approx 3$–8 s. In the flap mono array (Fig. 18(b)), arrayed flaps generally underperform the isolated device, indicating predominantly destructive interactions. In contrast, mixed-array PAs (Fig. 18(c)) absorb more power than the isolated PA over the 3–5 s range, while mixed-array flaps (Fig. 18(d)) exhibit substantially higher absorption than mono-flap counterparts over 3–8 s. This demonstrates that improved q-factors arise from coherent and complementary hydrodynamic interactions across a broad period range, rather than isolated peak responses.

At 90° (Fig. 19), all arrayed devices underperform their isolated counterparts. PA mono arrays (Fig. 19(a)) show systematic losses, particularly near the primary response peak. Flap mono arrays (Fig. 19(b)) absorb negligible power due to perpendicular incidence. Mixed-array PAs (Fig. 19(c)) and flaps (Fig. 19(d)) similarly show no enhancement, confirming that without favourable wave–array alignment, hydrodynamic coupling suppresses individual device performance and overall array efficiency.

4. Discussion

Heterogeneity enhances resilience in complex systems by enabling diverse components to fulfil complementary roles. Within wave energy, this idea has been explored through heterogeneous WEC arrays [17,18], which vary size or draft within a fixed device type, and through hybrid arrays combining different working principles within the same dominant degree of freedom [14,15].

With this work, we explore an alternative direction that considers both varying geometries and WECs operating in different dominant DOFs, so that their radiated wave fields are structurally distinct rather than scaled versions of the same pattern. Mixed configurations of this type, where devices differ in geometry, dominant DOF, and working principle simultaneously, have received less dedicated attention than the heterogeneous and same-DOF hybrid cases. The present study applies the same hydrodynamic solver to both mono and mixed configurations so that performance differences are attributable solely to array composition.

The results reveal several distinct advantages of mixed arrays. Most prominently, they exhibit superior directional robustness: whereas mono-flap arrays suffer near-total efficiency collapse at perpendicular incidence, mixed arrays maintain stable power absorption across all wave angles due to the complementary response characteristics of their constituent devices. Mixed configurations also frequently outperform mono arrays on a per-unit-width basis, confirming that gains stem from genuine hydrodynamic synergies (constructive cross-coupling and favourable radiated wave-field alignment) rather than from increased physical footprint.

These findings carry direct implications for deployment. The observation of q- and M-factors exceeding unity suggests that mixed arrays could increase effective capacity factors, enabling target energy outputs with fewer devices and reduced capital expenditure and spatial requirements. The latter is particularly significant in contested shallow-water environments.

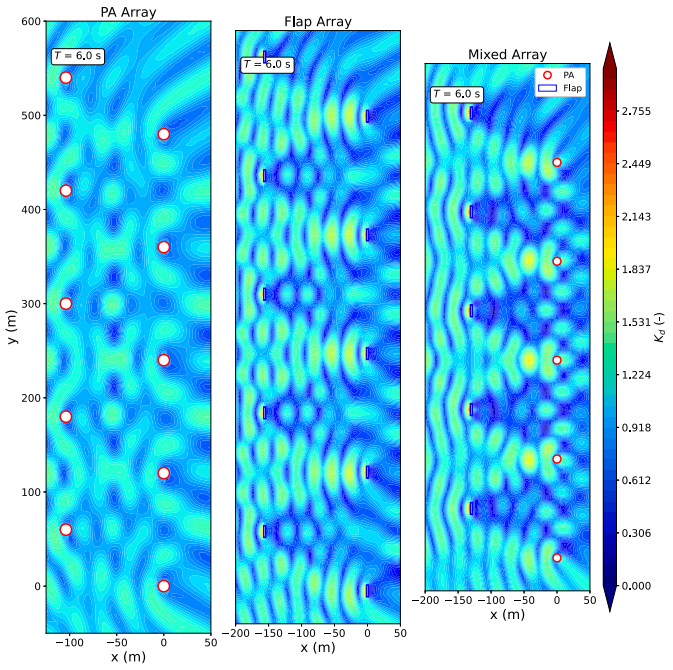

(a) $T = 6\,\mathrm{s}$

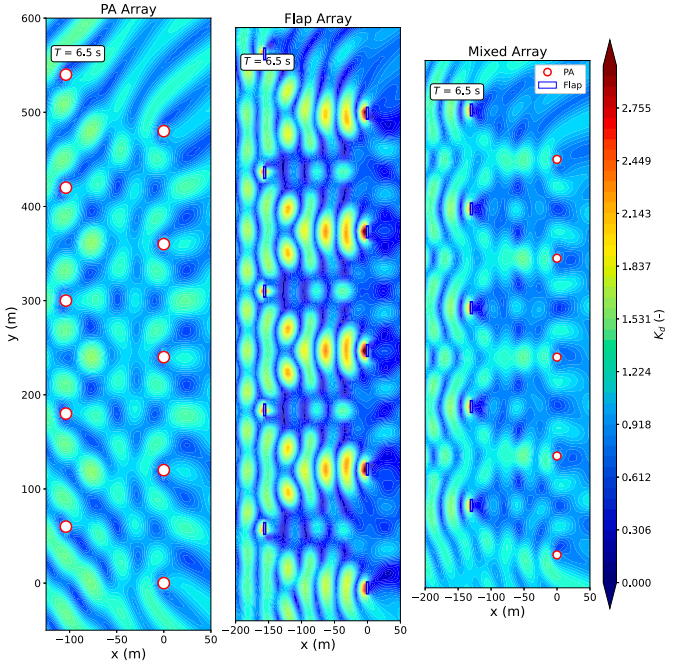

(b) $T = 6.5\,\mathrm{s}$

Fig. 14. Disturbance coefficient K_d for mixed and mono arrays (the incoming wave direction is from left to right).

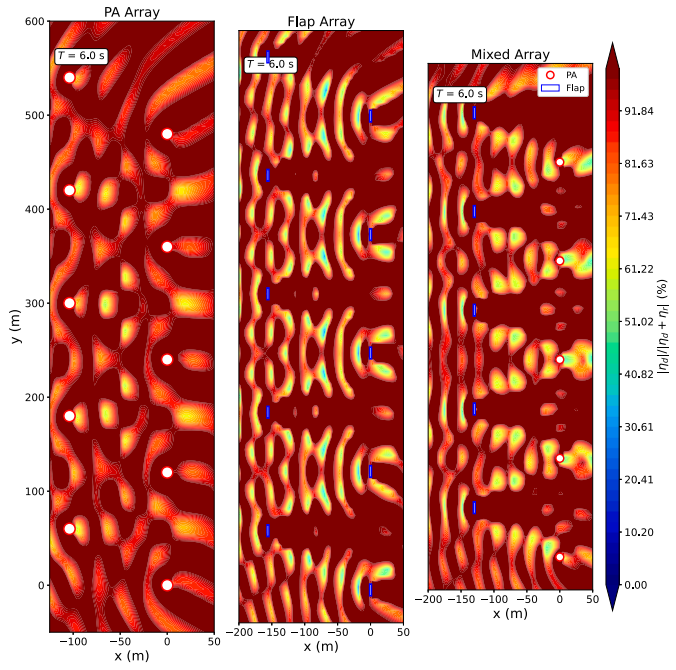

(a) Percentage diffraction in perturbed wave field

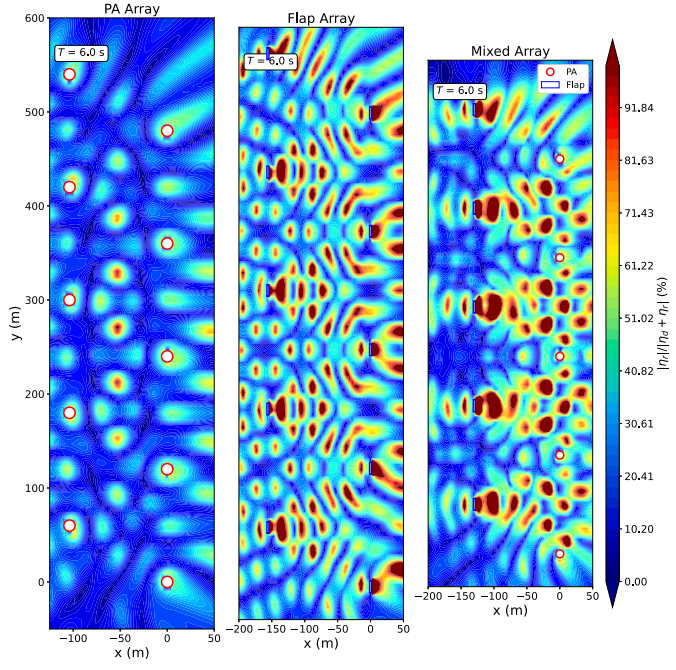

(b) Percentage radiation in perturbed wave field

Fig. 15. Percentage contributions of the diffraction and radiation to the perturbed wave field at T = 6 s (The incoming wave direction is from left to right).

Placed in the context of the existing literature, these findings extend prior work in several specific ways. Heterogeneous PA studies have reported gains over mono-arrays ranging from 2.9% [16] to 6.6–20.02% [18] and up to 37–72.2% with control co-design under multi-directional wind-waves [17]; the mixed PA–flap configurations examined here reach peak q-factors of 1.6 under regular waves and mean values up to 1.22 under irregular waves with active control. The mechanism, however, is different: rather than tuning device size, the mixed configurations exploit the complementary radiation patterns of heave-dominated PAs and pitch-dominated flaps, producing a directional robustness (non-zero q-factor at 90° and 270°) that heterogeneous PA studies cannot in principle reproduce, since they vary geometry within a single dominant DOF.

For hybrid arrays, Zheng et al. [14] reported H-factor values as high as 1.6 for OWC–PA combinations; the M-factor introduced here (Section 2.2) serves as a per-unit-width complement to the H-factor that becomes meaningful when device characteristic widths differ substantially, and reaches peak values of 2.25 for the small PA–flap configuration. The directional-robustness mechanism is also distinct from

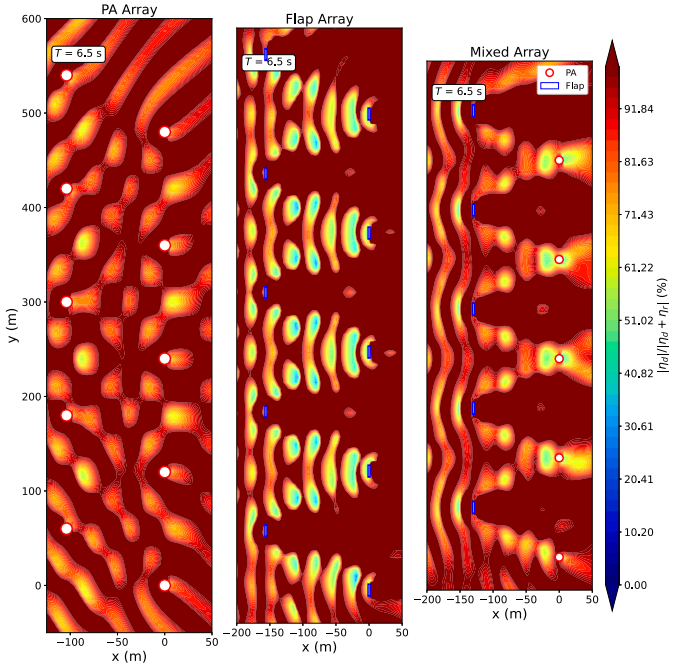

(a) Percentage diffraction in perturbed wave field

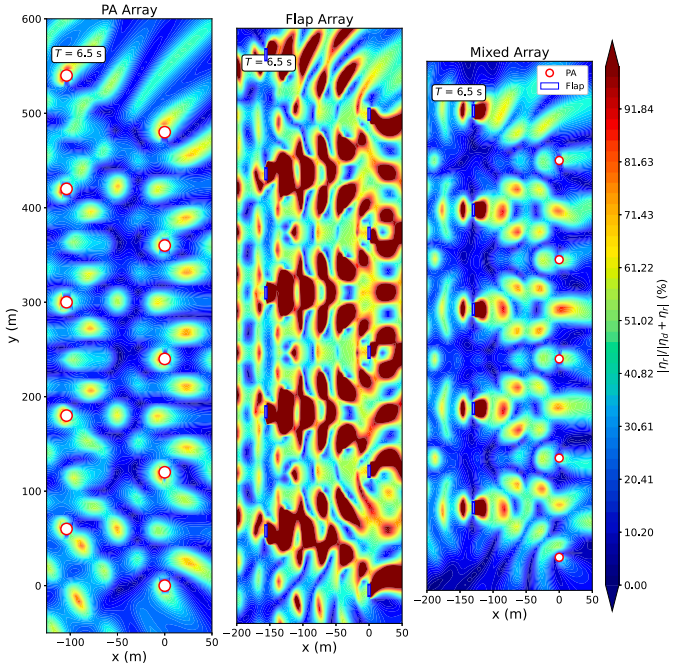

(b) Percentage radiation in perturbed wave field

Fig. 16. Percentage contributions of the diffraction and radiation to the perturbed wave field at $T = 6.5$ s (The incoming wave direction is from left to right).

the spatial-diversity enhancements reported for PA arrays in front of reflecting walls [19,20] and from the modal-coupling enhancements within multi-DOF devices such as the Mocean attenuator [21]: it operates at the device-class level rather than at the device-position or intra-device-mode level, and is therefore complementary to those mechanisms. Building on the preliminary analysis of Raghavan et al. 2025 [22], the configuration space examined here is substantially broader (3360 cases), and the analysis identifies geometric efficiency, in addition to power gain, as a design lever specific to mixed configurations that previous studies do not address.

Despite the comprehensive scope of this study, several limitations remain. The weakly non-linear frequency-domain formulation may not be applicable to extreme sea states, where transient and strongly non-linear effects require a time-domain model; future work should therefore incorporate time-domain simulations to assess survivability, control performance, and fatigue loading in mixed arrays. For single flap devices, performance is evaluated only for the dominant wave direction, and extending this directional treatment to array-level q- and M-factor assessments would provide less conservative estimates. The present PTO models, under both passive and active control, do not impose explicit force limits, which become increasingly important at higher sea states; incorporating direct force constraints within the control formulation would improve physical realism. For active control specifically, explicitly accounting for the energy expended in real time, including reverse energy flow and PTO actuator efficiency, would allow a more complete assessment of net power absorption.

Beyond these methodological extensions, the in-depth hydrodynamic interpretation in this paper is anchored in regular-wave results because monochromatic forcing isolates resonant interactions and radiation-pattern interference cleanly. Irregular-wave conditions are also analysed throughout, with q- and M-factor results reported alongside the regular-wave figures, but the underlying mechanisms are not interpreted at the same depth in the irregular case. This asymmetry has consequences: resonant peaks at specific periods (e.g. $T = 6$ s for the small PA–flap mixed array) are sharper in regular waves than under realistic spectra; the collapse of mono-flap arrays to $q = 0$ at perpendicular incidence is similarly sharper in unidirectional regular waves than under directional spread, so the relative robustness advantage of mixed arrays at these directions is less stark in practice than the regular-wave figures alone suggest; and the active-control figures, including the constrained-heave amplification reported above, should be read as upper bounds achievable by an idealised displacement-aware controller rather than as values realisable by a real-time controller under stochastic forcing. A natural step that would deepen the irregular-wave treatment is the computation of site-integrated annual energy production (AEP), weighting the absorbed-power matrix obtained here for irregular sea states by the joint H_s–T_p probability distribution from the ECHOWAVE hindcast at the site.

5. Conclusions

This work focuses on "mixed" wave energy arrays, examining 3360 cases comparing mono-arrays of PAs or flaps against mixed PA–flap configurations through interaction-based (q-factor) and geometry-normalised (M-factor) metrics. Mixed arrays outperform mono arrays by combining the direction-dependent energy extraction of flaps with the isotropic response of point absorbers, yielding higher average q-factors than PA mono-arrays (and, for several configurations, exceeding flap mono-arrays) with greater directional robustness and reduced sensitivity to array size. M-factor analysis confirms that the gains arise from genuine hydrodynamic interactions rather than from device size alone. In a 10-device staggered mixed array at $T = 6.0$ s, predominantly constructive radiation-damping cross-coupling produces a peak q-factor of 1.6 and M-factor of 2.25, with a 175% increase in PA heave RAOs and a 34% increase in flap excitation forces; the underlying driver in all such cases is the spacing-to-wavelength ratio governing wave-field coherence.

The same mechanisms can, however, induce severe penalties when wave-field coherence is disrupted: at $T = 6.5$ s, where spacing corresponds to a half-integer wavelength multiple, destructive interference reverses the sign of the radiation-damping cross-coupling, and although mixed arrays retain some power absorption at unfavourable angles where mono-flap arrays fail entirely, performance remains sensitive to layout choices. Under irregular waves these effects are spectrally

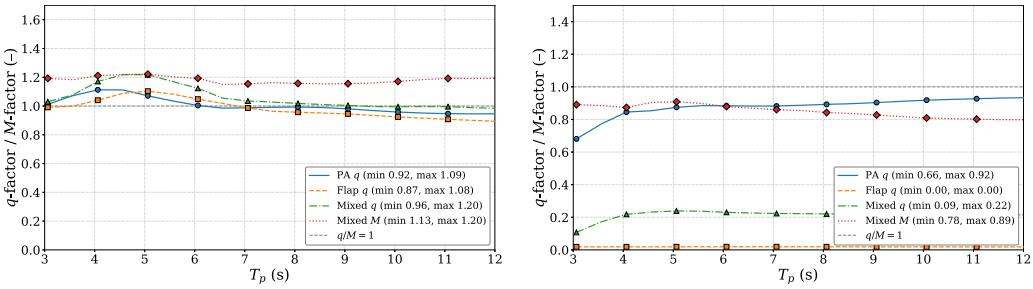

(a) Incident angle 0° (b) Incident angle 90°

Fig. 17. q-factors for the mono and mixed arrays and M-factor for mixed arrays with passive control under irregular waves.

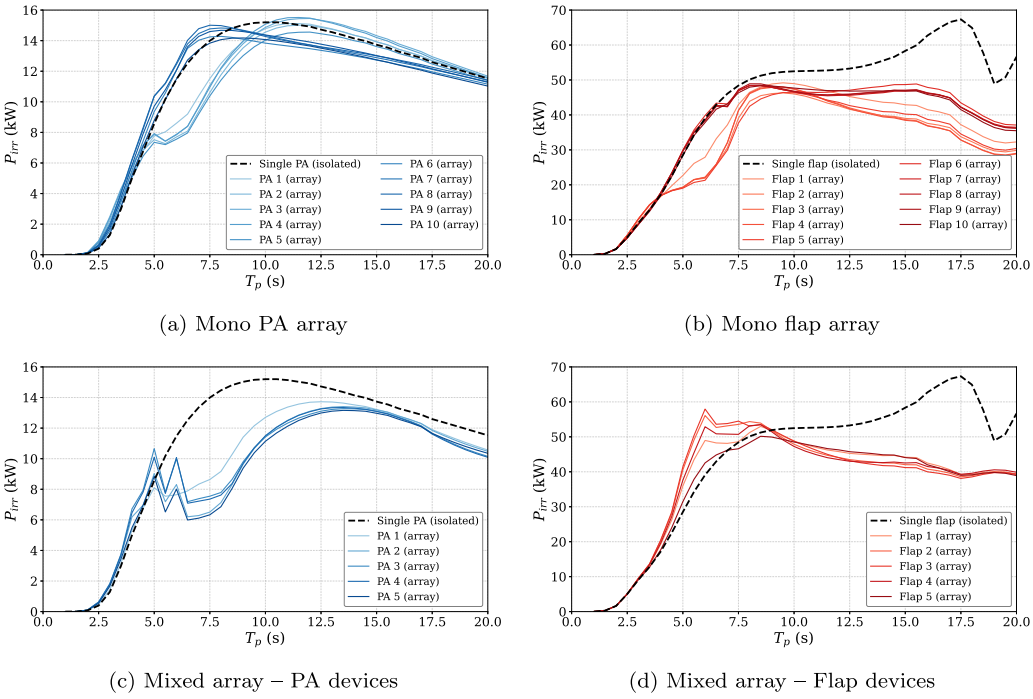

(a) Mono PA array (b) Mono flap array

(c) Mixed array – PA devices (d) Mixed array – Flap devices

Fig. 18. Power absorption of individual devices at 0° incident wave under passive control in irregular waves.

smoothed but remain operative, with mixed configurations sustaining M-factors above unity across a wide range of peak periods. The findings confirm that mixed PA–flap arrays offer a robust alternative to mono-device arrays and provide the physical foundation for the techno-economic analyses needed to translate hydrodynamic gains into reduced LCOE and optimised array footprints.

CRediT authorship contribution statement

Vaibhav Raghavan: Writing – original draft, Visualization, Validation, Supervision, Software, Methodology, Investigation, Formal analysis, Data curation, Conceptualization. **Andrei V. Metrikine:** Writing – review & editing, Supervision. **George Lavidas:** Writing – review & editing, Resources, Project administration, Funding acquisition, Conceptualization.

Declaration of competing interest

The authors declare that they have no known competing financial interests or personal relationships that could have appeared to influence the work reported in this paper.

Acknowledgements

The authors would also like to acknowledge SURF and access to the HPC Snellius for running the simulations in HAMS-MREL, under project EINF3290. The solver HAMS-MREL can be found here (DOI:10.4121/1ba9ae9a-c1d5-4886-ada8-33072e4dff7d).

Appendix

A.1. Hydrodynamic modelling of single devices

At 15 m water depth, dominant sea states have $T_p \approx 5$–6 s and $H_s \approx 1$ m (Fig. 1(b)). Radiation damping and PTO control broaden the 6 m PA's bandwidth to 3–12 s despite its 3.6 s natural period. This low-energy climate supports a weakly non-linear approach with viscous drag for both control strategies.

The PA heave equation at ω_i, neglecting PTO and viscous effects, is (Eq. (A.1)):

$$[-\omega_i^2(m_d + m_a(\omega_i)) + i\omega_i b_a(\omega_i) + c_h]\,\zeta(\omega_i) = f_e(\omega_i) \tag{A.1}$$

where m_d, m_a, b_a, c_h, f_e, ζ denote dry mass, added mass, radiation damping, hydrostatic stiffness, excitation force, and displacement amplitude; the RAO is $\bar{\zeta} = \zeta/a$.

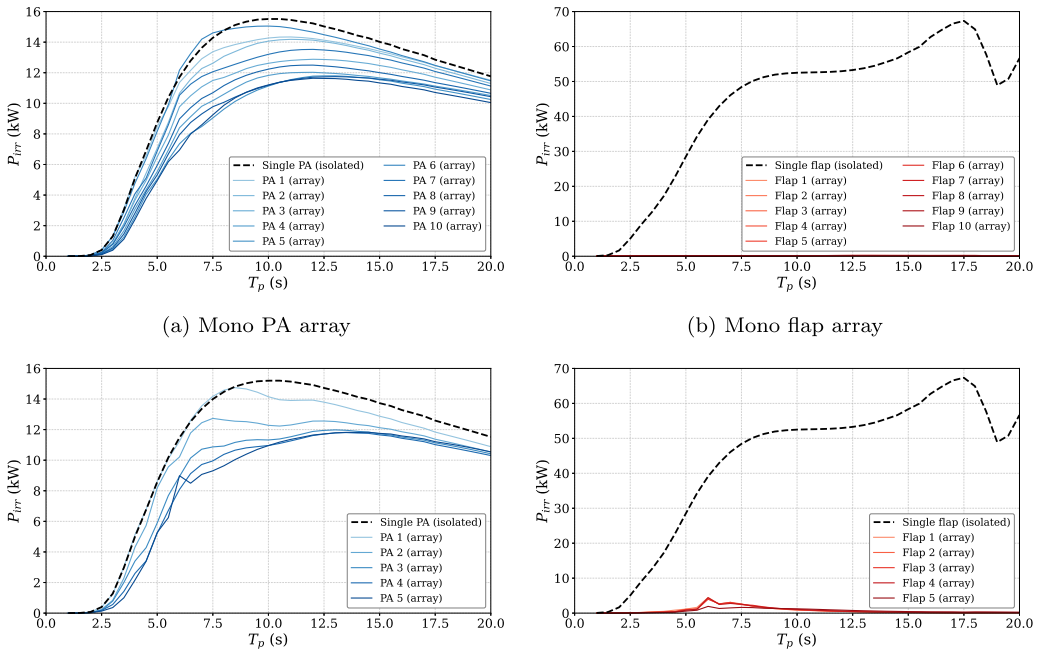

(a) Mono PA array (b) Mono flap array

(c) Mixed array – PA devices (d) Mixed array – Flap devices

Fig. 19. Power absorption of individual devices at 90° incident wave under passive control in irregular waves.

The flap pitch equation is (Eq. (A.2)):

$$[-\omega_i^2(I_d + I_a(\omega_i)) + i\omega_i B_a(\omega_i) + C_h]\theta(\omega_i) = M_e(\omega_i) \tag{A.2}$$

with analogous pitch quantities and $\bar{\theta} = \theta/a$. Natural periods follow from peak RAO response. Hydrodynamic coefficients are computed with HAMS-MREL [24], using generalised modes for the flap.

A.1.1. Passive control

The PTO maximises absorbed power via frequency-dependent damping [35], with forces (Eq. (A.3)):

$$F_{PTO}(\omega_i) = i\omega_i b_{PTO}(\omega_i)\zeta(\omega_i), \quad M_{PTO}(\omega_i) = i\omega_i B_{PTO}(\omega_i)\theta(\omega_i) \tag{A.3}$$

Optimal damping [35] (Eq. (A.4)):

$$b_{PTO}(\omega_i) = \sqrt{R(\omega_i)^2 + X(\omega_i)^2} \tag{A.4}$$

with (Eq. (A.5)):

$$R(\omega_i) = b_a(\omega_i) + b_v, \qquad X(\omega_i) = i\omega_i[m_d + m_a(\omega_i)] + \frac{c_h}{i\omega_i} \tag{A.5}$$

Including PTO and viscous damping (Eq. (A.6)):

$$[-\omega_i^2(m_d + m_a(\omega_i)) + i\omega_i(b_a(\omega_i) + b_{PTO}(\omega_i) + b_v) + c_h]\,\zeta(\omega_i) = f_e(\omega_i) \tag{A.6}$$

$C_D = 1.7$ is used for the flap [26]. For the PAs, $KC = 2\pi\zeta/D$ stays between 1 and 3 at $H = 2$ m, supporting $C_D = 0.5$ [25,27,36]

For regular waves, viscous damping follows Lorentz linearisation [21] (Eq. (A.7)):

$$b_v = \frac{4}{3\pi} C_D \rho A_D \tag{A.7}$$

with ρ the fluid density and A_D the projected area. Power per frequency is $P(\omega_i) = \frac{1}{2}\, b_{PTO}\, \omega_i^2\, |\zeta_i|^2$.

For irregular waves, a weakly non-linear frequency-domain method [37] tunes b_{PTO} to $T_e = m_{-1}/m_0$. An iterative scheme updates b_v via (Eq. (A.8)) [38]:

$$b_v = \tfrac{1}{2}\,\rho\, C_D\, A_D\, \sigma_u \sqrt{8/\pi} \tag{A.8}$$

until MSE between successive response vectors falls below 10^{-6}. Absorbed power is (Eq. (A.9)):

$$P_{\text{irr}} = \eta \int_0^\infty 2P(\omega)\, S(\omega)\, \mathrm{d}\omega \tag{A.9}$$

where $S(\omega)$ is a Goda-type spectrum [37] and $\eta = 0.9$ [39,40]. Structural-velocity statistical linearisation is used for the flap, since relative-velocity formulations add complexity with only 5%–10% power difference [27].

A.1.2. Active control

The active scheme of Fusco and Ringwood [41], extended by Ermakov et al. [17], varies PTO impedance to align velocity with excitation, theoretically maximising power [35]. Displacement constraints are imposed; the PA formulation below applies equally to the flap.

The force–displacement relation is (Eq. (A.10)):

$$\zeta(\omega_i) = \frac{f_{\text{ex}}(\omega_i) + f_{\text{PTO}}(\omega_i)}{i\omega_i Z(\omega_i)} \tag{A.10}$$

with intrinsic impedance [42]:

$$Z(\omega_i) = b_a(\omega_i) + b_v + i\omega_i \left(m_d + m_a(\omega_i) - \frac{c_h}{\omega_i} \right) \tag{A.11}$$

The complex-conjugate law $F_{\text{PTO}}(\omega_i) = i\omega_i Z^*(\omega_i)\zeta(\omega_i)$ yields:

$$V(\omega) = \frac{1}{2(b_a(\omega_i) + b_v)}\, F_{\text{exc}}(\omega). \tag{A.12}$$

This non-causal law is approximated by assuming a narrow-banded excitation with amplitude, frequency, and phase estimated through an Extended Kalman Filter [43]:

$$f_{ex}(t) = A(t)\cos(\omega t + \varphi(t)). \tag{A.13}$$

A parameter α enforces displacement limits [17]. The PTO impedance is:

$$Z_{PTO} = (2\alpha - 1)d - ie \tag{A.14}$$

where d, e are the real and imaginary parts of Z. The displacement:

$$\zeta = \frac{f_{ex}}{2i\omega_i \alpha x} \tag{A.15}$$

with:

$$\text{If } |\zeta| > \zeta_{max}, \text{ then } \alpha = \frac{|\zeta|}{\zeta_{max}}. \tag{A.16}$$

Regular-wave power is (Eq. (A.17)):

$$P(\omega_i) = \frac{1}{2} Z_{PTO}\, \omega_i^2\, |\zeta_i|^2. \tag{A.17}$$

Maximum displacements are 0.3× draft (PAs) and 15° (flap). Under irregular waves:

$$P_{\text{irr}} = \int_0^\infty P(\omega) p_{ss}(\omega)\, d\omega, \qquad p_{ss}(\omega) = \frac{S(\omega)}{\int_0^\infty S(\omega) d\omega}. \tag{A.18}$$

EKF estimates update Z_{PTO} quasi-statically over each dominant wave cycle, so mean power is set by the resistive PTO term while reactive terms only store energy temporarily.

Constrained motion reverses about 10%–40% of PTO power [41]. With efficiency η [39,40], the net electrical ratio is:

$$\boxed{\frac{P_{\text{net},\eta}}{P_{\text{net},100}} = \frac{\eta - Q/\eta}{1 - Q}} \tag{A.19}$$

where $Q = P_{\text{rev}}/P_{\text{abs}}$. For $\eta = 0.9$, $Q = 0.2$, the ratio is ≈0.847, i.e. 85% of ideal; this is the effective efficiency under active control.

A.2. Hydrodynamic modelling of arrays

The n-device equation of motion at ω_i is (Eq. (A.20)):

$$\left[-\omega_i^2 (\mathbf{M}_d + \mathbf{M}_a(\omega_i)) + i\omega_i \left(\mathbf{B}_a(\omega_i) + \mathbf{B}_{\text{PTO}}(\omega_i) + \mathbf{B}_v\right) + \mathbf{C}_h\right] \boldsymbol{\zeta}(\omega_i) = \mathbf{F}_e(\omega_i), \tag{A.20}$$

where $\mathbf{M}_d$, $\mathbf{C}_h$, $\mathbf{B}_v$ are diagonal, $\mathbf{M}_a$ and $\mathbf{B}_a$ are fully populated, and $\mathbf{B}_{PTO}$, $\mathbf{F}_e$, $\boldsymbol{\zeta}$ complete the system. The intrinsic impedance matrix is (Eq. (A.21)):

$$\mathbf{Z}(\omega_i) = \mathbf{B}_a(\omega_i) + \mathbf{B}_v + i\omega_i \left[\mathbf{M}_d + \mathbf{M}_a(\omega_i) - \frac{\mathbf{C}_h}{\omega_i}\right], \tag{A.21}$$

with entries (Eq. (A.22)):

$$\mathbf{Z} = \begin{pmatrix} d_{1,1} + je_{1,1} & \dots & d_{1,n} + je_{1,n} \\ \vdots & \ddots & \vdots \\ d_{n,1} + je_{n,1} & \dots & d_{n,n} + je_{n,n} \end{pmatrix}, \tag{A.22}$$

where $d_{i,j}$ combines radiation and viscous damping; $e_{i,j}$ combines added mass and hydrostatic terms.

A.2.1. Passive control for arrays

Following [44,45], the experimentally validated optimal PTO matrix is (Eq. (A.23)):

$$\mathbf{B}_{PTO}(\omega_i) = \left[\left(\mathbf{B}_a(\omega_i) + \mathbf{B}_v\right)^2 + \left(\omega_i\left(\mathbf{M}_d + \mathbf{M}_a(\omega_i)\right) - \frac{\mathbf{C}_h}{\omega_i}\right)^2\right]^{1/2}. \tag{A.23}$$

For irregular waves, the same spectral iteration (MSE = 10^{-6}) gives per-device b_v. Array power is (Eq. (A.24)):

$$P_{\text{array}}(\omega_i) = \frac{1}{2}\eta\, \omega_i^2\, \boldsymbol{\zeta}^*(\omega_i)\, \mathbf{B}_{PTO}(\omega_i)\, \boldsymbol{\zeta}(\omega_i), \tag{A.24}$$

and for irregular waves (Eq. (A.25)):

$$P_{\text{irr}} = \int_0^\infty 2\, P(\omega)\, S(\omega)\, d\omega. \tag{A.25}$$

A.2.2. Active control for arrays (Array SAE)

The Array SAE controller [17], validated against MPC for mono arrays, gives (Eq. (A.26)) [42]:

$$\boldsymbol{\zeta}(\omega_i) = \frac{1}{i\omega_i}\, \mathbf{Z}^{-1}(\omega_i) \cdot \left[\mathbf{F}_{ex}(\omega_i) + \mathbf{F}_{PTO}(\omega_i)\right]. \tag{A.26}$$

The global PTO impedance is (Eq. (A.27)):

$$\mathbf{Z}_{pto} = \begin{pmatrix} (2\alpha_1 - 1)d_{1,1} - je_{1,1} & \dots & (2\alpha_n - 1)d_{1,n} - je_{1,n} \\ \vdots & \ddots & \vdots \\ (2\alpha_1 - 1)d_{n,1} - je_{n,1} & \dots & (2\alpha_n - 1)d_{n,n} - je_{n,n} \end{pmatrix}, \tag{A.27}$$

with α_i enforcing motion limits. The total $\mathbf{H} = \mathbf{Z} + \mathbf{Z}_{\text{pto}}$ is (Eq. (A.28)):

$$\mathbf{H} = \begin{pmatrix} 2\alpha_1 d_{1,1} & \dots & 2\alpha_n d_{1,n} \\ \vdots & \ddots & \vdots \\ 2\alpha_1 d_{n,1} & \dots & 2\alpha_n d_{n,n} \end{pmatrix}. \tag{A.28}$$

Displacements are (Eq. (A.29)):

$$\boldsymbol{\zeta} = \begin{pmatrix} \frac{1}{2i\omega\alpha_1}\left(\sum_{i=1}^n \frac{C_{i,1} F_i}{|\mathbf{H}|}\right) \\ \vdots \\ \frac{1}{2i\omega\alpha_n}\left(\sum_{i=1}^n \frac{C_{i,1} F_i}{|\mathbf{H}|}\right) \end{pmatrix}, \tag{A.29}$$

constrained by (Eq. (A.30)) [42]:

$$\text{If } |\zeta_i| > \zeta_{\text{Max}} \rightarrow \alpha_i = \frac{|\zeta_i|}{\zeta_{\text{Max}}}. \tag{A.30}$$

The time-averaged power is (Eq. (A.31)):

$$\begin{aligned} \mathbf{P}(\omega_i) &= \frac{1}{2}\,\text{Re}\left(\mathbf{Z}_{\text{pto}}(\omega_i)\right)\, \omega_i^2 |\boldsymbol{\zeta}(\omega_i)|^2 \\ &= \frac{1}{2}\begin{pmatrix} (2\alpha_1 - 1)d_{1,1}(\omega_i) & \dots & (2\alpha_n - 1)d_{1,n}(\omega_i) \\ \vdots & \ddots & \vdots \\ (2\alpha_1 - 1)d_{n,1}(\omega_i) & \dots & (2\alpha_n - 1)d_{n,n}(\omega_i) \end{pmatrix} \\ &\quad \times \omega_i^2 \begin{pmatrix} |\zeta_1(\omega_i)|^2 \\ \vdots \\ |\zeta_n(\omega_i)|^2 \end{pmatrix}. \end{aligned} \tag{A.31}$$

This frequency-domain formulation is computationally efficient and needs no convergence check for power.

References

[1] Iván A. Hernández-Robles, Xiomara González-Ramírez, Julián A. Gómez-Gutiérrez, Juan M. Ramirez, Wave power assessment for electricity generation with powerbouy system by wave motion emulation modelling, Sustain. Energy Technol. Assess. (ISSN: 2213-1388) 43 (2021) 100962, http://dx.doi.org/10.1016/j.seta.2020.100962, URL https://www.sciencedirect.com/science/article/pii/S2213138820313904.

[2] Tsunamis behave as shallow-water waves, 2017, URL https://www.geological-digressions.com/tsunamis-behave-as-shallow-water-waves/. (Accessed 25 August 2023).

[3] Kester Gunn, Clym Stock-Williams, Quantifying the global wave power resource, Renew. Energy (ISSN: 0960-1481) 44 (2012) 296–304, http://dx.doi.org/10.1016/j.renene.2012.01.101, URL https://www.sciencedirect.com/science/article/pii/S0960148112001310.

[4] S. Astariz, G. Iglesias, The economics of wave energy: A review, Renew. Sustain. Energy Rev. (ISSN: 1364-0321) 45 (2015) 397–408, http://dx.doi.org/10.1016/j.rser.2015.01.061, URL https://www.sciencedirect.com/science/article/pii/S1364032115000714.

[5] G. Lavidas, L. Mezilis, M. Alday, H. Baki, J. Tan, A. Jain, T. Engelfried, V. Raghavan, Marine renewables in energy systems: Impacts of climate data, generators, energy policies, opportunities, and untapped potential for 100% decarbonised systems, Energy (ISSN: 0360-5442) 336 (2025) 138359, http://dx.doi.org/10.1016/j.energy.2025.138359.

[6] Jakob Bru, Tom Stian Seland, Jian Dai, Zhiyu Jiang, Life cycle cost analysis of an offshore floating photovoltaic concept in the North Sea, Renew. Energy (ISSN: 0960-1481) 249 (2025) 122981, http://dx.doi.org/10.1016/j.renene.2025.122981, URL https://www.sciencedirect.com/science/article/pii/S0960148125006433.

[7] Markel Penalba, Imanol Touzón, Joseba Lopez-Mendia, Vincenzo Nava, A numerical study on the hydrodynamic impact of device slenderness and array size in wave energy farms in realistic wave climates, Ocean Eng. (ISSN: 0029-8018) 142 (2017) 224–232, http://dx.doi.org/10.1016/j.oceaneng.2017.06.047, URL https://www.sciencedirect.com/science/article/pii/S0029801817303517.

[8] Silvia Bozzi, Marianna Giassi, Adrià Moreno Miquel, Alessandro Antonini, Federica Bizzozero, Giambattista Gruosso, Renata Archetti, Giuseppe Passoni, Wave energy farm design in real wave climates: the Italian offshore, Energy (ISSN: 0360-5442) 122 (2017) 378–389, http://dx.doi.org/10.1016/j.energy.2017.01.094, URL https://www.sciencedirect.com/science/article/pii/S0360544217301019.

[9] Malin Göteman, Jens Engström, Mikael Eriksson, Jan Isberg, Optimizing wave energy parks with over 1000 interacting point-absorbers using an approximate analytical method, Int. J. Mar. Energy (ISSN: 2214-1669) 10 (2015) 113–126, http://dx.doi.org/10.1016/j.ijome.2015.02.001, URL https://www.sciencedirect.com/science/article/pii/S2214166915000119.

[10] Philip Balitsky, Nicolas Quartier, Gael Verao Fernandez, Vasiliki Stratigaki, Peter Troch, Analyzing the near-field effects and the power production of an array of heaving cylindrical WECs and OSWECs using a coupled hydrodynamic-PTO model, Energies (ISSN: 1996-1073) 11 (12) (2018) http://dx.doi.org/10.3390/en11123489, URL https://www.mdpi.com/1996-1073/11/12/3489.

[11] Zhi Yung Tay, Vengatesan Venugopal, Hydrodynamic interactions of oscillating wave surge converters in an array under random sea state, Ocean Eng. (ISSN: 0029-8018) 145 (2017) 382–394, http://dx.doi.org/10.1016/j.oceaneng.2017.09.012, URL https://www.sciencedirect.com/science/article/pii/S0029801817305310.

[12] J. Cameron McNatt, Vengatesan Venugopal, David Forehand, A novel method for deriving the diffraction transfer matrix and its application to multi-body interactions in water waves, Ocean Eng. (ISSN: 0029-8018) 94 (2015) 173–185, http://dx.doi.org/10.1016/j.oceaneng.2014.11.029, URL https://www.sciencedirect.com/science/article/pii/S0029801814004417.

[13] J. Cameron McNatt, Aaron Porter, Kelley Ruehl, Comparison of numerical methods for modeling the wave field effects generated by individual wave energy converters and multiple converter wave farms, J. Mar. Sci. Eng. (ISSN: 2077-1312) 8 (3) (2020) http://dx.doi.org/10.3390/jmse8030168, URL https://www.mdpi.com/2077-1312/8/3/168.

[14] Siming Zheng, Yongliang Zhang, Gregorio Iglesias, Power capture performance of hybrid wave farms combining different wave energy conversion technologies: The H-factor, Energy (ISSN: 0360-5442) 204 (2020) 117920, http://dx.doi.org/10.1016/j.energy.2020.117920, URL https://www.sciencedirect.com/science/article/pii/S0360544220310276.

[15] Siming Zheng, Yongliang Zhang, Gregorio Iglesias, Wave–structure interaction in hybrid wave farms, J. Fluids Struct. (ISSN: 0889-9746) 83 (2018) 386–412, http://dx.doi.org/10.1016/j.jfluidstructs.2018.09.012, URL https://www.sciencedirect.com/science/article/pii/S0889974618302937.

[16] Malin Göteman, Wave energy parks with point-absorbers of different dimensions, J. Fluids Struct. (ISSN: 0889-9746) 74 (2017) 142–157, http://dx.doi.org/10.1016/j.jfluidstructs.2017.07.012, URL https://www.sciencedirect.com/science/article/pii/S0889974617301627.

[17] Andrei M. Ermakov, Zain Anwar Ali, Kumars Mahmoodi, Oliver Mason, John V. Ringwood, Optimisation of heterogeneous wave energy converter arrays: A control co-design strategy, Renew. Energy (ISSN: 0960-1481) 244 (2025) 122637, http://dx.doi.org/10.1016/j.renene.2025.122637, URL https://www.sciencedirect.com/science/article/pii/S096014812500299X.

[18] Habeebullah Abdulkadir, Ossama Abdelkhalik, Optimization of heterogeneous arrays of wave energy converters, Ocean Eng. (ISSN: 0029-8018) 272 (2023) 113818, http://dx.doi.org/10.1016/j.oceaneng.2023.113818, URL https://www.sciencedirect.com/science/article/pii/S0029801823002020.

[19] Ai-Jun Li, Yong Liu, Xinyu Wang, Hydrodynamic performance of vertical cylindrical wave energy absorbers in front of a vertical wall, Phys. Fluids 36 (2024) http://dx.doi.org/10.1063/5.0194206.

[20] Amy-Rose Westcott, Luke G. Bennetts, Nataliia Y. Sergiienko, Benjamin S. Cazzolato, Broadband near-perfect capture of water wave energy by an array of heaving buoy wave energy converters, J. Fluid Mech. 998 (2024) A5, http://dx.doi.org/10.1017/jfm.2024.819.

[21] J. McNatt, Christopher Retzler, The performance of the Mocean M100 wave energy converter described through numerical and physical modelling, Int. Mar. Energy J. 3 (2020) 11–19, http://dx.doi.org/10.36688/imej.3.11-19.

[22] Exploring the hydrodynamics of Mixed Wave Energy farms, in: Proceedings of the European Wave and Tidal Energy Conference, Vol. 16, 2025, http://dx.doi.org/10.36688/ewtec-2025-699, URL https://publications.evolvingcities.org/proc-ewtec/article/view/699.

[23] Matías Alday, George Lavidas, The ECHOWAVE Hindcast: A 30-years high resolution database for wave energy applications in North Atlantic European waters, Renew. Energy (ISSN: 0960-1481) 236 (2024) 121391, http://dx.doi.org/10.1016/j.renene.2024.121391, URL https://www.sciencedirect.com/science/article/pii/S0960148124014599.

[24] V. Raghavan, E. Loukogeorgaki, N. Mantadakis, A.V. Metrikine, G. Lavidas, HAMS-MREL, a new open source multiple body solver for marine renewable energies: Model description, application and validation, Renew. Energy (ISSN: 0960-1481) 237 (2024) 121577, http://dx.doi.org/10.1016/j.renene.2024.121577, URL https://www.sciencedirect.com/science/article/pii/S0960148124016458.

[25] Xinyuan Shao, Jonas W. Ringsberg, Hua-Dong Yao, Uday Rajdeep Sakleshpur Lokesh Gowda, Hrishikesh Nitin Khedkar, Jørgen Hals Todalshaug, Hydrodynamic interactions and enhanced energy harnessing amongst many WEC units in large-size wave parks, J. Mar. Sci. Eng. (ISSN: 2077-1312) 12 (5) (2024) http://dx.doi.org/10.3390/jmse12050730, URL https://www.mdpi.com/2077-1312/12/5/730.

[26] Pauline Laporte Weywada, D1.1 advanced wave-structure interaction model – theory and user manual, Zenodo (2018) http://dx.doi.org/10.5281/zenodo.2562765.

[27] Leandro S.P. da Silva, Benjamin S. Cazzolato, Nataliia Y. Sergiienko, Boyin Ding, Helio M. Morishita, Celso P. Pesce, Statistical linearization of the morison's equation applied to wave energy converters, J. Ocean. Eng. Mar. Energy (ISSN: 2198-6452) 6 (2) (2020) 157–169, http://dx.doi.org/10.1007/s40722-020-00165-9.

[28] Giuseppe Giorgi, John V. Ringwood, Nonlinear Froude-Krylov and viscous drag representations for wave energy converters in the computation/fidelity continuum, Ocean Eng. (ISSN: 0029-8018) 141 (2017) 164–175, http://dx.doi.org/10.1016/j.oceaneng.2017.06.030, URL https://www.sciencedirect.com/science/article/pii/S0029801817303256.

[29] Jian Tan, George Lavidas, A modified spectral-domain model for nonlinear hydrostatic restoring force of heaving wave energy converters, Ocean Eng. (ISSN: 0029-8018) 309 (2024) 118581, http://dx.doi.org/10.1016/j.oceaneng.2024.118581, URL https://www.sciencedirect.com/science/article/pii/S002980182401919X.

[30] A. Babarit, J. Hals, M.J. Muliawan, A. Kurniawan, T. Moan, J. Krokstad, Numerical benchmarking study of a selection of wave energy converters, Renew. Energy (ISSN: 0960-1481) 41 (2012) 44–63, http://dx.doi.org/10.1016/j.renene.2011.10.002, URL https://www.sciencedirect.com/science/article/pii/S0960148111005672.

[31] Jannik Meyer, Christian Windt, Philipp Sinn, Arndt Hildebrandt, On the mooring methodology of heaving point absorber arrays, Ocean Eng. (ISSN: 0029-8018) 281 (2023) 114659, http://dx.doi.org/10.1016/j.oceaneng.2023.114659, URL https://www.sciencedirect.com/science/article/pii/S0029801823010430.

[32] Steffen Marburg, Six boundary elements per wavelength: is that enough? J. Comput. Acoust. 10 (01) (2002) 25–51, http://dx.doi.org/10.1142/S0218396X02001401, arXiv:https://doi.org/10.1142/S0218396X02001401.

[33] Dezhi Ning, Xiaojie Su, Ming Zhao, Bin Teng, Numerical study of resonance induced by wave action on multiple rectangular boxes with narrow gaps, Acta Ocean. Sin. (ISSN: 1869-1099) 34 (5) (2015) 92–102, http://dx.doi.org/10.1007/s13131-015-0672-1.

[34] V. Raghavan, Andrei Metrikine, George Lavidas, Exploring the hydrodynamics of mixed wave energy farms, in: Proceedings of the European Wave and Tidal Energy Conference, (EWTEC 2025), Vol. 16, 2025, http://dx.doi.org/10.36688/ewtec-2025-699, Paper 699.

[35] Jorgen Hals, Torkel Bjarte-Larsson, Johannes Falnes, Optimum reactive control and control by latching of a Wave-Absorbing semisubmerged heaving sphere, in: International Conference on Offshore Mechanics and Arctic Engineering, in: volume 21st International Conference on Offshore Mechanics and Arctic Engineering, Vol. 4, 2002, pp. 415–423, http://dx.doi.org/10.1115/OMAE2002-28172, arXiv:https://asmedigitalcollection.asme.org/OMAE/proceedings-pdf/OMAE2002/36142/415/4545242/415_1.pdf.

[36] Jørgen Todalshaug, A. Babarit, Jorgen Krokstad, Made J. Muliawan, Adi Kurniawan, Torgeir Moan, The NumWEC project. Numerical estimation of energy delivery from a selection of wave energy converters – final report, 2015, http://dx.doi.org/10.13140/RG.2.1.3807.8885.

[37] M. Alday, V. Raghavan, G. Lavidas, Effects of wave spectrum representation on power production estimations from point absorbers, Appl. Ocean Res. (ISSN: 0141-1187) 161 (2025) 104626, http://dx.doi.org/10.1016/j.apor.2025.104626.

[38] Jian Tan, Wei Tao, Antonio Jarquin Laguna, Henk Polinder, Yihan Xing, Sape Miedema, A spectral-domain wave-to-wire model of wave energy converters, Appl. Ocean Res. (ISSN: 0141-1187) 138 (2023) 103650, http://dx.doi.org/10.1016/j.apor.2023.103650, URL https://www.sciencedirect.com/science/article/pii/S0141118723001918.

[39] T. Strager, A. Martin dit Neuville, P. Fernández López, G. Giorgio, T. Mureşan, P. Andersen, K.M. Nielsen, T.S. Pedersen, E. Vidal Sánchez, Optimising Reactive Control in Non-Ideal Efficiency Wave Energy Converters, in: International Conference on Offshore Mechanics and Arctic Engineering, Vol. 9A: Ocean Renewable Energy, 2014, V09AT09A002, http://dx.doi.org/10.1115/OMAE2014-23005, arXiv:https://asmedigitalcollection.asme.org/OMAE/proceedings-pdf/OMAE2014/45530/V09AT09A002/4432200/v09at09a002-omae2014-23005.pdf.

[40] Romain Genest, Félicien Bonnefoy, Alain H. Clément, Aurélien Babarit, Effect of non-ideal power take-off on the energy absorption of a reactively controlled one degree of freedom wave energy converter, Appl. Ocean Res. (ISSN: 0141-1187) 48 (2014) 236–243, http://dx.doi.org/10.1016/j.apor.2014.09.001, URL https://www.sciencedirect.com/science/article/pii/S0141118714000893.

[41] Francesco Fusco, John V. Ringwood, A simple and effective Real-Time controller for wave energy converters, IEEE Trans. Sustain. Energy 4 (1) (2013) 21–30, http://dx.doi.org/10.1109/TSTE.2012.2196717.

[42] Johannes Falnes, Adi Kurniawan, Ocean Waves and Oscillating Systems: Linear Interactions Including Wave-Energy Extraction, vol. 8, Cambridge University Press, 2020.

[43] Francesco Fusco, John V. Ringwood, Short-Term wave forecasting for Real-Time control of wave energy converters, IEEE Trans. Sustain. Energy 1 (2) (2010) 99–106, http://dx.doi.org/10.1109/TSTE.2010.2047414.

[44] Johannes Falnes, Radiation impedance matrix and optimum power absorption for interacting oscillators in surface waves, Appl. Ocean Res. (ISSN: 0141-1187) 2 (2) (1980) 75–80, http://dx.doi.org/10.1016/0141-1187(80)90032-2, URL https://www.sciencedirect.com/science/article/pii/0141118780900322.

[45] Timothy Vervaet, Nicolas Quartier, Efrain Carpintero Moreno, Gael Verao Fernandez, Francesco Ferri, Vasiliki Stratigaki, Peter Troch, System identification and centralised causal impedance matching control of a row of two heaving point absorber wave energy converters, Ocean Eng. (ISSN: 0029-8018) 309 (2024) 118399, http://dx.doi.org/10.1016/j.oceaneng.2024.118399, URL https://www.sciencedirect.com/science/article/pii/S0029801824017372.